

EXPERIMENTAL INVESTIGATION OF FLUIDIZED BED TO BE USED AS
SOLAR THERMAL ENERGY STORAGE

A THESIS SUBMITTED TO
THE GRADUATE SCHOOL OF NATURAL AND APPLIED SCIENCES
OF
MIDDLE EAST TECHNICAL UNIVERSITY

BY

ESRA POLAT

IN PARTIAL FULFILLMENT OF THE REQUIREMENTS
FOR
THE DEGREE OF MASTER OF SCIENCE
IN
MECHANICAL ENGINEERING

AUGUST 2019

Approval of the thesis:

**EXPERIMENTAL INVESTIGATION OF FLUDIZED BED TO BE USED
AS SOLAR THERMAL ENERGY STORAGE**

submitted by **Esra Polat** in partial fulfillment of the requirements for the degree of
**Master of Science in Mechanical Engineering Department, Middle East
Technical University** by,

Prof. Dr. Halil Kalıpçılar
Dean, Graduate School of **Natural and Applied Sciences**

Prof. Dr. Sahir Arıkan
Head of Department, **Mechanical Engineering**

Prof. Dr. İlker Tarı
Supervisor, **Mechanical Engineering Dept., METU**

Examining Committee Members:

Prof. Dr. H. Tuba Okutucu Özyurt
Mechanical Engineering Dept., METU

Prof. Dr. İlker Tarı
Mechanical Engineering Dept., METU

Assist. Prof. Dr. Özgür Bayer
Mechanical Engineering Dept., METU

Prof. Dr. Cemil Kocar
Nuclear Engineering Dept., Hacettepe University

Prof. Dr. Murat Köksal
Mechanical Engineering Dept., Hacettepe University

Date: 27.08.2019

I hereby declare that all information in this document has been obtained and presented in accordance with academic rules and ethical conduct. I also declare that, as required by these rules and conduct, I have fully cited and referenced all material and results that are not original to this work.

Name, Surname: ESRA POLAT

Signature :

ABSTRACT

EXPERIMENTAL INVESTIGATION OF FLUIDIZED BED TO BE USED AS SOLAR THERMAL ENERGY STORAGE

Polat, Esra
MSc., Department of Mechanical Engineering
Supervisor: Prof. Dr. İlker Tari

August 2019, 71 pages

An air-granular particle fluidized bed system with dimensions of 0.08 m x 0.4 m x 0.08 m designed and analyzed experimentally and modeled with a commercial CFD software. The aim of the hydrodynamic and thermal experiments is validation of the numerical model previously developed by Serdar Hiçdurmaz. For this purpose, an experimental setup is built at METU and CFD model of Hiçdurmaz is modified for the new geometry with the same solution settings. First-order time discretization and Eulerian-Eulerian approach are used in the model. Syamlal O'Brien drag model and Gunn thermal model are applied. Silica sand from Geldart B type particles is used in both experimental and numerical studies. After sand particles, all experimental studies are repeated with sintered bauxite particles, which are called CARBOHSP, to compare the behaviors of different particles in the fluidized bed system. Experimental results of pressure drop and bed height expansion are used for validating the CFD model. During thermal experiments, 585 K hot sand is used and, with K-type thermocouples, temperatures are measured and compared with the simulation results. Both hydrodynamical and thermal experimental results are consistent with the CFD results.

Keywords: Thermal Energy Storage, Bubbling Fluidized Bed, Multiphase Flow

ÖZ

ISI ENERJİ DEPOSU OLARAK KULLANILAN YATAKLARIN DENEYSEL İNCELENMESİ

Polat, Esra
Yüksek Lisans, Makine Mühendisliği Bölümü
Tez Danışmanı: Prof. Dr. İlker Tarı

Ağustos 2019, 71 sayfa

Hava ve granüller tanecikli yapıdaki, 0.08 m x 0.4 m x 0.08 m boyutlarında tasarlanan ısı enerjisi depolama ünitesi, deneysel ve hesaplamalı akışkanlar dinamiği yazılımı yardımıyla incelenmiştir. Hidrodinamik ve ısıl deneyler Serdar Hıçdurmaz'ın [19][29] sayısal çalışmasını doğrulamak amacıyla yapılmıştır. Bu amaç doğrultusunda ODTÜ'de deney düzeneği kurulup Hıçdurmaz'ın modeli yeni geometri ve aynı çözüm yollarıyla tekrar modellenmiştir. Modelde birinci derece zaman ayrıştırma tercih edilmiş ve Eulerian-Eulerian yaklaşımı kabul edilmiştir. Modelleme çalışması boyunca Syamlal-O'Brien sürüklenme modeli ve Gunn termal modeli kullanılmıştır. Her iki çalışmada da Geldart B tanecik tipindeki silika kum kullanılmıştır. Bütün deneyler kum taneciklerinden sonra tezde CARBOHSP olarak anılan sinterlenmiş boksit tanecikleriyle farklı parçacıkların akışkan yatak içindeki davranışlarını karşılaştırmak için tekrar edilmiştir. Yatak boyunca basınç düşümü ve yatak yükselme oranının deneysel sonuçları yazılım değerleri ile doğrulanmıştır. Isıl deneyler sırasında 585 K sıcaklığında kum kullanılıp sıcaklık değerleri K tipi ısıölçerler ile ölçülüp model verileri ile kıyaslanmıştır. Her iki deneyin sonuçları da model sonuçları ile tutarlılık göstermiştir.

Anahtar Kelimeler: Isı Enerji Deposu, Kabarcıklı Akışkan Yatak, Çok Fazlı Akış

to my beloved family

ACKNOWLEDGMENTS

First of all, I would like to express my sincere gratitude to Prof. Dr. İlker Tarı for his motivation, contributions, and sensitivity from beginning to the end of my thesis.

Secondly, I am thankful to Serdar Hiçdurmaz for sharing his knowledge and experience with me during all of the study.

Additionally, I am grateful to Mustafa Yalçın for his precious support in experimental studies.

Finally, my family deserves appreciation for their encouragement, patience, and warm support.

TABLE OF CONTENTS

ABSTRACT.....	v
ÖZ	vi
ACKNOWLEDGMENTS.....	viii
TABLE OF CONTENTS	ix
LIST OF TABLES	xi
LIST OF FIGURES.....	xii
LIST OF SYMBOLS	xv
1.INTRODUCTION.....	1
1.1 Motivation.....	1
1.2 Concentrated Solar Power Systems	3
1.3 Thermal Energy Storage Systems for CSP Applications.....	5
1.4 Granular Particles as Heat Storage Medium.....	7
1.5 Phenomenon of Fluidization.....	9
1.5.1 Bubbling Fluidized Bed	12
1.5.2 Geldart’s Classic Classification of Particles	13
1.6 Thesis Overview	15
2.EXPERIMENTAL STUDY	17
2.1 Hydrodynamic Experiments	17
2.2 Thermal Experiments.....	25
2.3 Expected Uncertainty.....	29
3.CFD MODEL DEVELOPMENT.....	31
3.1 Physical Components of the CFD Model	31
3.1.1 Solid Particle	31
3.1.2 Fluidization Gas	32

3.1.3 Bed Geometry	32
3.2 Solution Approach.....	33
3.2.1 Mesh Refinement Study.....	37
3.2.2 Time Step Optimization.....	39
4.RESULTS AND DISCUSSION	41
4.1 Hydrodynamic Results	41
4.1.1 Pressure Drop.....	41
4.1.2 Bed Expansion Ratio	46
4.2 Thermal Results.....	49
4.2.1 Temperature Gradient	49
4.2.2 Heat Transfer Coefficient Between Phases	53
4.2.3 Heat Transfer Analysis Between Phases	55
5.CONCLUSIONS.....	59
5.1. Future Work.....	61
REFERENCES	63
APPENDICES	67
A. Experimental Temperature (K) Variation of Sand Particles at Different Elevations for First 340 s , U=0.38	67

LIST OF TABLES

TABLES

Table 1. Parameters of physical model.....	33
Table 2. Important velocities of different particles.....	45

LIST OF FIGURES

FIGURES

Figure 1.1 PV Panel Volume and Generation in United States	2
Figure 1.2 CSP Volume and Generation in United States	2
Figure 1.3 Four main technologies for CSP generation (parabolic through system, power tower system, dish system, linear Fresnel system)	4
Figure 1.4 Schematic of power tower CSP system integrated with molten salt heat storage	7
Figure 1.5 Illustrated CSP system with fluidized-bed thermal energy storage	8
Figure 1.6 Various forms of batch of solids by contacting fluid	10
Figure 1.7 Bubble schematic in bubbling fluidized bed	13
Figure 1.8 Geldart classification of the particles diagram	14
Figure 2.1 Schematic of hydrodynamic experimental setup	18
Figure 2.2 Real look of hydrodynamic experimental setup	19
Figure 2.3 Schematic drawing of bed	20
Figure 2.4 Real view of bed with sand and CARBOHSP particles	21
Figure 2.5 Air compressor	23
Figure 2.6 Rotameter and pressure regulator	24
Figure 2.7 Furnace	26
Figure 2.8 Schematic of thermal experimental setup	27

Figure 2.9 Real view of thermal experimental set-up	28
Figure 3.1 Heat loss points through the outside of the bed	36
Figure 3.2 Mesh setting for computational domain	38
Figure 3.3 Temporal bed heights for various mesh sizes.....	39
Figure 3.4 Temporal pressure drop variation for different time steps.....	40
Figure 4.1 Theoretical change of pressure drop with superficial velocity.....	42
Figure 4.2 Pressure drop across the bed change with superficial gas velocity.....	43
Figure 4.3 Pressure drop inside the bed at different experimental studies.....	44
Figure 4.4 Pressure drop inside the bed ($P_{y=0,025\ m} - P_{y=0,39\ m}$)	44
Figure 4.5 Experimental pressure drop variation with different granular particles ($P_{y=0,025\ m} - P_{y=0,39\ m}$)	46
Figure 4.6 Experimental and simulated bed expansion ratio of sand particles for different velocities	47
Figure 4.7 Experimental bed expansion ratios of sand and CARBOHSP particles.	48
Figure 4.8 Similar views of bubbles in experimental and CFD studies	48
Figure 4.9 Temperature variation of phases at first 60 s in CFD results at $y=0.10\ m$ and $u=0.38\ m/s$	50
Figure 4.10 Air temperature variations of experimental and CFD results at $u=0.46$ m/s and $y=0.10\ m$	50
Figure 4.11 Experimental air temperature values at different elevations, $u=0.46\ m/s$	51

Figure 4.12 Experimental air temperature variation of fluidized bed with sand and CARBOHSP particles when $u=0.38$ m/s and $y=0.10$ m52

Figure 4.13 Real attitude of interphase heat transfer coefficient ($u=0.38$ m/s)53

Figure 4.14 Interphase heat transfer coefficient change with time from CFD results at different elevations.....54

Figure 4.15 Experimental variation of the air exit temperature at $u=0.46$ m/s and $y=0.10$ m.....55

Figure 4.16 Heat transfer efficiency between phases for different studies.....57

LIST OF SYMBOLS

SYMBOLS

A	Interfacial area concentration, m^2
A_{eq}	Perfect sphere surface area, m^2
A_p	Surface area of particle, m^2
C_p	Specific heat capacity, $J/kg-K$
C_D	Drag coefficient, -
d_s	Particle diameter, m
e_{SS}	Restitution coefficient, -
h	Interphase heat transfer coefficient, W/m^2K
h_{air}	Air heat transfer coefficient, W/m^2K
H	Bed height, m
H_0	Initial bed height, m
K_{gs}	Momentum transfer coefficient, -
k_g	Thermal conductivity of air, W/mK
k_{ins}	Thermal conductivity of insulator, W/mK
k_{steel}	Thermal conductivity of stainless steel, W/mK
Nu_s	Nusselt number for solid particles, -
Pr	Prandtl number, -
P_y	Pressure at specified elevation, kPa
Q_{int}	Volumetric rate of heat transfer, W
Re_s	Reynolds number for particles, -

Re_{mf}	Reynolds number at minimum fluidization, -
$T_{ins,o}$	Temperature of outside of insulation, K
$T_{w,i}$	Temperature of wall inside, K
$T_{w,o}$	Temperature of wall outside, K
T_{∞}	Temperature of ambient, K
U_{mf}	Minimum fluidization velocity, m/s
U_T	Terminal velocity, m/s
u	Superficial velocity, m/s
V_p	Particle volume, m^3
v_g	Velocity of gas, m/s
v_s	Velocity of solid, m/s
y	Specified elevation, m
ε_s	Volume fraction of solid, -
ε_g	Volume fraction of gas, -
μ_g	Dynamic viscosity of the gas, $kg/m-s$
ρ_g	Density of gas, kg/m^3
ρ_s	Density of solid, kg/m^3
τ	Stress tensor, Pa
ϕ	Sphericity, -

CHAPTER 1

INTRODUCTION

1.1 Motivation

We have relied on burning fossil fuels to generate energy for quite a long time. However, using coal, gas, and oil for our needs is causing a problem in today's world. One of the greatest environmental challenges is climate change, and our addiction to fossil fuels is the main cause behind it. Even though we act like there is a limitless available amount of these energy resources, actually they are fast running out. Renewable energy is the answer to these problems, and solar energy is a promising candidate with other clean energy suppliers. Solar energy can be operated by current technologies as directly or indirectly. Wind, wave, low grade geothermal and tidal are examples of indirect solar energy sources. Direct solar energy source includes solar rays and they can be converted to useful energy by two different technologies: solar photovoltaics (also known as PV) and solar thermal energy systems (STEs). The main difference between solar photovoltaics and STE is in their working principles. PV technology directly converts sunlight into electricity using panels made of the semiconductor (such as silicon-monocrystalline, and amorphous) cells [1]. Herewith, PV technology can be operated only when the sun is available. Even though PV panels have reduced costs for some time now, this technology has a significant drawback, which is that energy can't be stored without high energy storage costs. Second solar power technology, Concentrated Solar Power systems (CSP) focus on the heating ability of solar rays. The concentrated sun light can be directly used as a heat source or used to drive a heat engine cycle. The most important advantage of CSP systems is that the heat can be stored in various media easily and cheaply so these systems may not be affected by the intermittent nature of the solar resource.

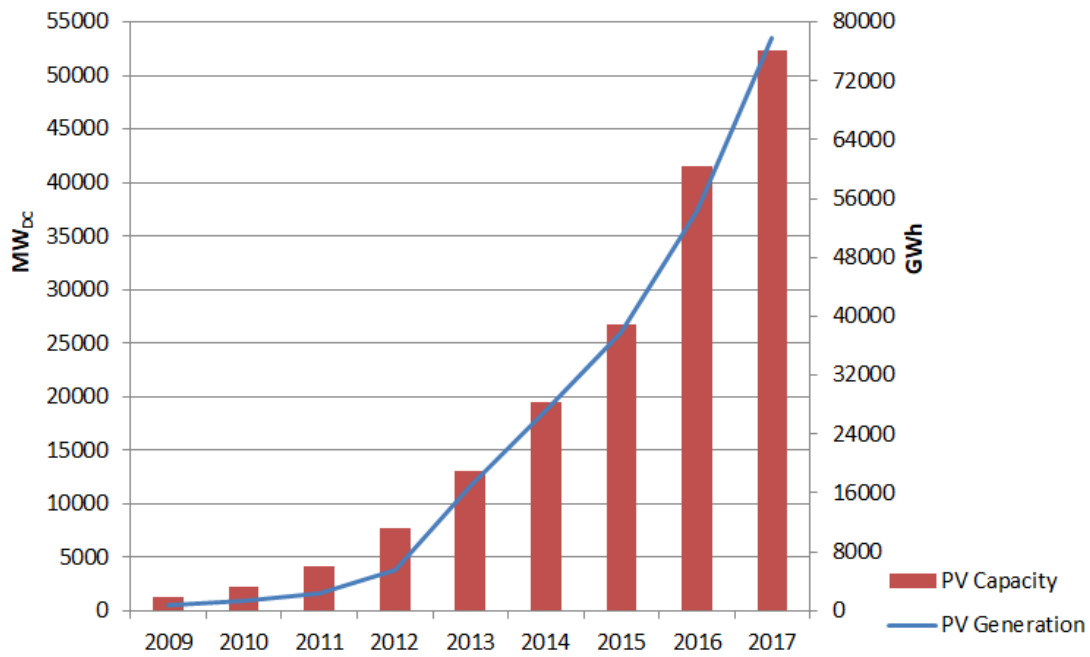


Figure 1.1 PV Panel Volume and Generation in the United States [3]

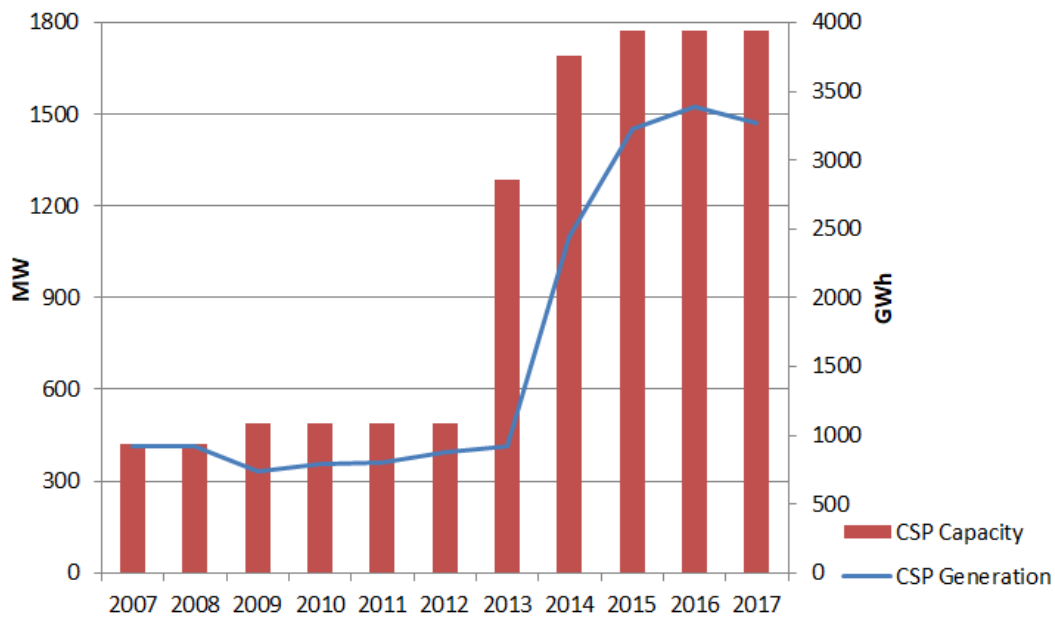


Figure 1.2 CSP Volume and Generation in the United States [3]

The reasons behind the spectacular rise in solar panels shown in Figure 1.1 are the money-savings, the low initial cost, the long lifetime of panels. Photovoltaic systems are more common in daily life because of their easy applicability at workplaces, solar farms and even in residential home use. Despite all, CSP systems still have a strong advantage because of their storage ability which should be further developed. In this study, the main aim is modeling and experimentally investigating a fluidized bed thermal energy storage unit. In the literature, there are many studies in the fluidization field. Most of them are numerical, and just a few experimental studies exist. This study includes many similarities to Taghipour's study [20]. A similar experimental set-up has been built and numerically supported. The difference between the experimental setups is the bed geometry. The most important factor which makes this study different from Taghipour's study is the thermal experimental study because he validated his numerical study only hydrodynamically.

1.2 Concentrated Solar Power Systems

The incident solar energy is not dense enough to obtain high temperatures. The working principle of CSP systems relies on focusing solar radiation using reflectors onto a receiver and transforming absorbed radiation to heat. In common applications, this heat is carried by a heat transfer fluid (HTF) to a steam or gas turbine, i.e., a heat engine to produce electricity. That heated HTF can also drive a thermochemical process. Solar rays may be concentrated with two different methods. The first one is the point focusing system; the second one is the line focusing system. In applications, parabolic trough and linear Fresnel collectors are examples of line focusing systems. In contrast, solar tower and dish systems belong to point focusing technologies. The four main CSP systems are represented in Figure 1.3. Each CSP power generator technology has distinctive properties. They have different working fluids, operating temperatures, abilities to focus sunlight, compatibilities with the power cycles and costs.

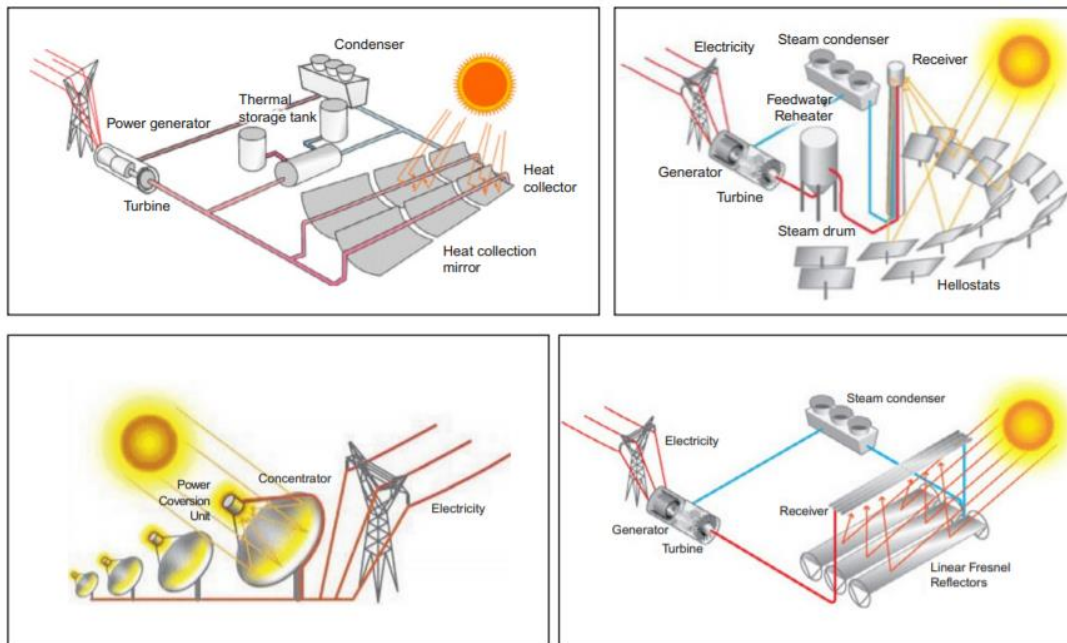


Figure 1.3 Four main technologies for CSP generation (parabolic trough system, power tower system, dish system, linear Fresnel system) [4]

Parabolic Trough Collector (PTC) systems have very high concentration ability; these collectors can take HTF up to 500°C. These line focusing collectors have cylindrically shaped parabolic mirrors and these reflect the sun rays onto a tubular receiver positioned in the focus line of the parabola. This tubular receiver with HTF transfers the heat to related devices [5]. Among the line focusing systems, PTC systems have the best overall plant efficiency.

Linear Fresnel (LFR) systems work similar principles with PTC systems but, distinctively, they apply linear focusing instead of circular focusing. Although PTC systems show more widespread usage, LFR system collectors are cheaper. Mirrors may be flat or capable of bending with basic constructions. Thanks to this design simplicity, they allow the configuration in various types. At this point, their collector-reflector structures supply packing ability. LFR systems can supply a

wide range of temperatures, 200 °C to 500 °C. Higher values are under development [6].

The power tower system is an example of a central receiver or point focusing system. Diversely from line focusing systems, they become of multiple tracking mirrors (heliostats) and one center receiver which is installed on a tower. Because of the fixed position of center tower receiver there is a limitation for collecting sun lights but, to overcome that conflict receiver area is increased to reach necessary energy efficiencies so this system needs wide land use. According to HTF characteristics, power tower systems can produce up to 1000 °C.

Parabolic dish systems include a reflector with parabolic-shaped that focuses the lights at a point onto a receiver. This system supplies HTF with a similar temperature of power tower systems. As advantages, these systems have low mirror costs, high quality, the easy setting for their modular structures and balanced design [8]. Parabolic dishes are the most efficient solar to electricity technology due to their high concentration ability. As a disadvantage, their maintenance cost is high by the reason of required two-axis tracking system.

1.3 Thermal Energy Storage Systems for CSP Applications

Intermittent nature of solar energy necessitates incorporation with efficient thermal energy storage (TES) systems. The materials used for TES systems should have some characteristic properties for effectivity such as; high thermal conductivity, high specific heat, high latent heat, chemical stability, low volume change, low cost, non-toxic, easy availability [9]. These materials may be classified into three main groups according to the heat storage mechanism as sensible, latent and chemical.

Sensible heat storage materials store that energy of heat in their specific heat capacity. Water, thermal oils, molten salts, liquid metals, and earth materials are the

best examples for this group [9].

All materials have some advantages and drawbacks. When water is easy to achieve, has a low cost, and high specific heat capacity (C_p), it also has a high vapor pressure and leads to corrosion. Thermal oils have higher heat storage ability than water due to their wide range of operating temperatures (12 °C-400°C) and lower vapor pressure than water but have a high cost. If the operating temperature is higher, molten salt became the most popular choice (operating temperature up to 600 °C). They have high thermal stability at high working temperatures, high volumetric heat capacity, low vapor pressure but they have a high melting point and low fluidity (this increases the pump cost). A power plant illustration with molten salt heat storage system is seen in Figure 1.4 [10]. Earth materials are also used as heat storage materials. Besides storage, they can be direct contact with heat, so there is no heat exchanger cost. Also, they are available, cheap, non-toxic and non-flammable [9].

Latent heat storage materials store the heat while phase changing processes. The solid-liquid phase change is the most popular type due to the drawbacks of others like huge volume change between liquid-gas phases. In the organic category; paraffin, esters, alcohols, in inorganic category; salts, salts eutectics, salt hydrates, metals, and alloys are the examples. While latent heat storage materials have a high density of energy storage, they have low thermal conductivity [9].

Chemical heat storage systems use reactions to heat storage. Magnesium hydroxide, calcium chloride and aluminum sulfate are some suitable examples of chemical storage systems. These systems provide the highest capacity for thermal energy storage. The disadvantages of these systems are reactions occur slowly and that reaction materials may undergo sintering.

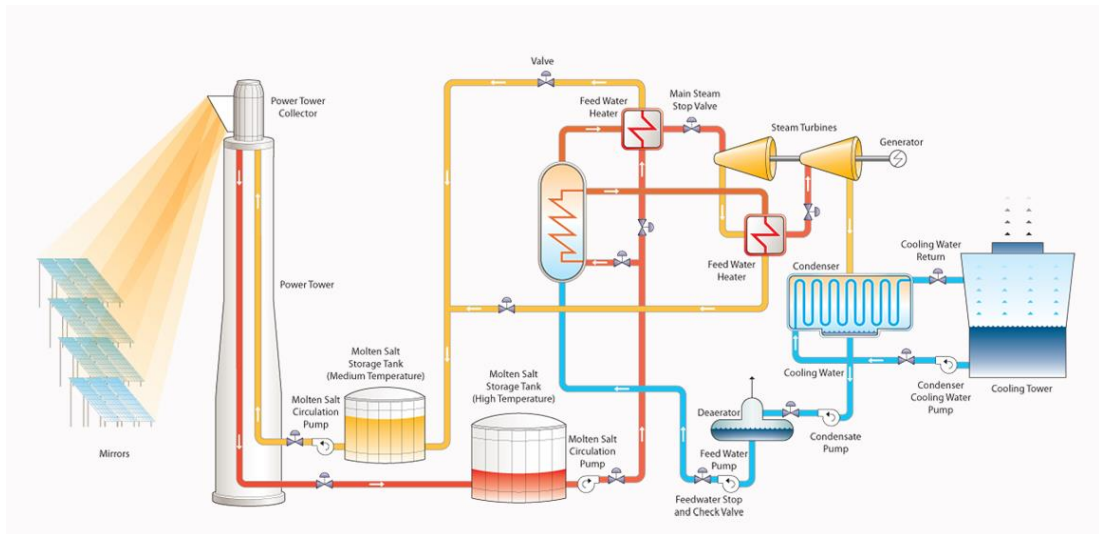


Figure 1.4 Schematic of power tower CSP system integrated with molten salt heat storage [10]

1.4 Granular Particles as Heat Storage Medium

Two tank molten-salt thermal energy storage systems are state-of-the-art TES systems in CSP technologies. Current molten salt storage systems face many difficulties; material stability at high temperatures (high operating temperature means high system efficiency), freezing of salt at low temperatures, material compatibility with metal-nonmetal materials at high temperatures, high salt and, silo costs. Granular solid particles can overcome these efficiency restricted factors. According to Ma et al. [11] investigation cost analysis specify that when particle-based TES systems costs less than $\$10/\text{kWh}_{\text{th}}$, molten salt-based TES systems cost more than double of it. In the same study, researchers indicated that fluidized bed TES systems can operate the system with higher than 800°C temperature and with over % 95 efficiency.

In the literature, solid particles were operated in TES systems with different techniques. In Warkerkar et al. [12] study air-sand HEX was examined with cross tubes. In spite of efficiency is high enough cracks were observed on the walls after a short time. In some other applications moving bed exchangers were studied [13]. The main drawback of this system is lower efficiency due to indirect heat exchange.

Fluidized bed (FB) system is one of the best solutions to utilize the advantages of solid particles. As shown in Figure 1.5, hot particles can be fluidized by compressed fluidizing gas and thermal energy in the system can be used for producing power. While selecting particles, material properties (heat capacity, particle size, and density), endurance ability, cost, and compatibility with fluidization should be considered. In the below system, cold particles move through the particle receiver to get heat by a lifting system. Hot particles fall into the hot silo and by help of a feeder enter to the FB-heat exchanger. After transferring their heat to fluidization gas, move through to a cold silo. The heated gas may drive a Rankine steam generator or a Brayton cycle.

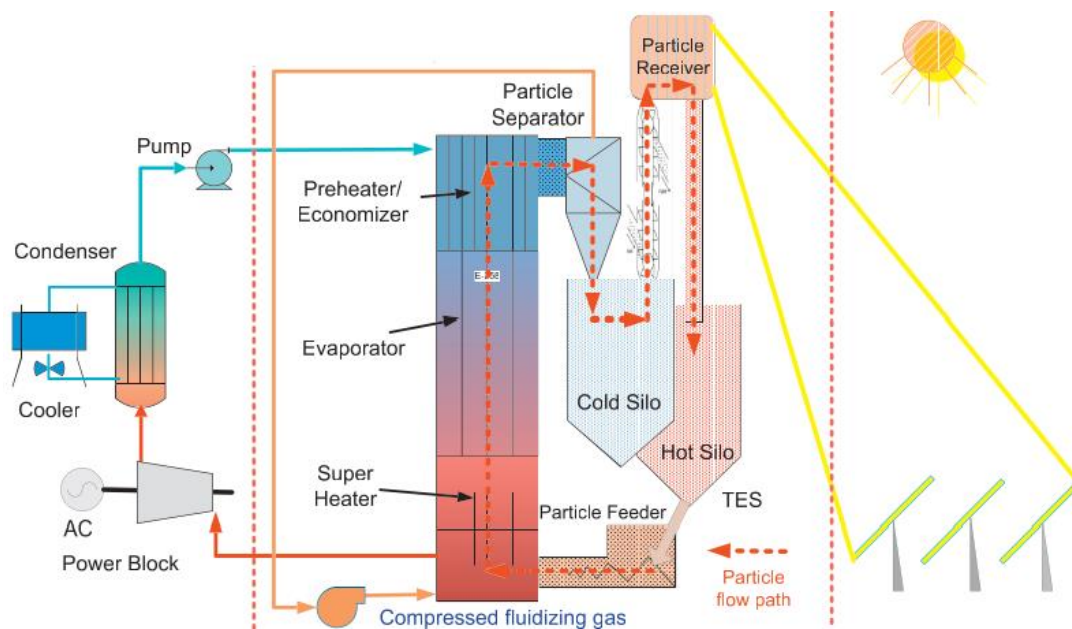


Figure 1.5 Illustrated CSP system with fluidized-bed thermal energy storage [11]

In this experimental study, silica sand is the granular material. Also, fluid is air in fluidization bed.

1.5 Phenomenon of Fluidization

Fluidization is a process that transforms granular solid particles into a fluidic state by help of gas or liquid medium. There are various forms of the batch of solid particles that contact a fluid. When the fluid moves through to the upper side of the bed with a low flow rate and if solid particles stay stable, this type called fixed bed and can be seen in Figure 1.6 (a). When the flow rate little increases, particles start to mobilize, and this form is called expanded bed. If flow rate continues to increase, at one point the drag force on particles and the weight of the particles come to a balance region. This region is called the minimum fluidization condition. Also, the velocity under this condition is named as velocity of minimum fluidization (U_{mf}) Figure 1.6 (b). After minimum fluidization, if flow rate increased and when the system includes liquid as a fluid bed passes to smooth fluidization regime Figure 1.6 (c). All regimes are not common for liquid and gas fluid types. After minimum fluidization, if the system is a gas-solid system bubbling is observed, Figure 1.6 (d). In extraordinary cases, in a solid-liquid system, if solid particles are very dense, bubbling may be observed. In solid-gas systems, if flow rate still increased and bed is high enough and not have large a diameter, bubble size increases and spreads across the vessel. This regime is called slugging Figure 1.6 (e). For coarse particles, slugging maybe occurs as flat slugging, as seen in Figure 1.6 (f). Again in a solid-gas system, if particles are fine enough and gas flow rate is quite high, the terminal velocity of the solids is exceeded and visible entrainment occurs. In this regime, bubbles turn to different shapes and sizes, and the turbulent motion of granular particles are observed. As shown in Figure 1.6 (g) this state named as turbulent fluidization. Finally if flow rate more increased, particles are moved through outside of the bed. That final state is called as lean phase fluidization and shown in Figure 1.6 (h).

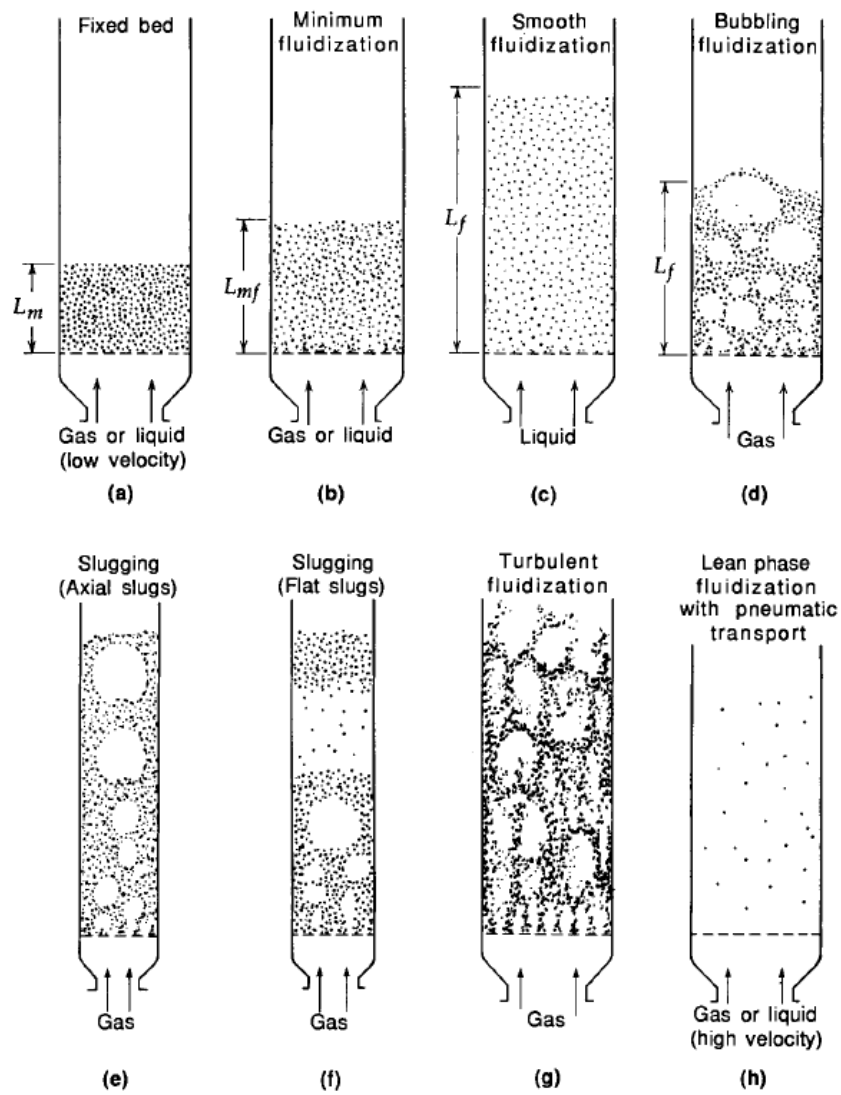


Figure 1.6 Various forms of batch of solids by contacting fluid [14]

The minimum fluidization velocity as follows [2]:

$$U_{mf} = \left(\frac{\mu_g Re_{mf}}{d_s \rho_g} \right) \quad (1)$$

Here Re_{mf} is Reynolds number in minimum fluidization conditions.

The terminal velocity, U_T which mentioned above is defined as a velocity at which all forces on the particle are in equilibrium and it can be expressed as;

$$U_T = \left(\frac{4d_s(\rho_s - \rho_g)g}{3\rho_g C_D} \right)^{1/2} \quad (2)$$

here C_D represents the drag coefficient.

Fluidization quality depends on different factors. The first is the size and shape of the granular solid particles. In fluidization, spherical shapes are demandable. Broadly, fine particles lead to clumping if they are moist, but if they are dry, they allow for satisfying fluidization at a wide range of gas flow rates.

In contrast, coarse particles are hard to fluidize. Generally slugging is observed, also in this uneven state structural damage may occur.

Besides solid material properties, gas phase properties are also important. Hydrodynamic properties of the gas, such as density and dynamic viscosity, directly affect the behavior of fluidization in gas-solid systems.

The second important factor is the density ratio of the bed. Liquid-solid mixtures tend to be homogenous but in solid-gas mixtures ratio is significant for fine fluidization. Besides these, bed geometry, the tendency of solids to clumping, and type of solids are some other factors.

Fluidized bed systems are useable for different industrial applications. Coal gasification, heat exchangers, gasoline production from other petroleum fractions, gasoline production from natural and synthesis gases, synthesis reactions, metallurgical processes, solidification, the coating of objects and drying of solids some important examples of these applications [14].

1.5.1 Bubbling Fluidized Bed

Fluidized bed system's efficiency is directly related to the ratio of interaction between different phases. In gas-solid systems flow regime of the gas through the bed and its heat transfer ability with the solid particles affects the performance. As mentioned earlier, after the minimum fluidization regime, one observes the bubbling fluidization. In this regime bed appears divided into two different phases; emulsion (dense regime) and bubbles. Bubble size, shape, and rising velocity are the important parameters for the characterization of a bubbling fluidized bed. Generally, bubbles are observed with Geldart A and B types of particles and mostly while bubbles are small with Geldart A-type particles they are bigger with Geldart B type. While designing a bubbling fluidized bed, superficial gas velocity should be set between U_{mf} and U_T .

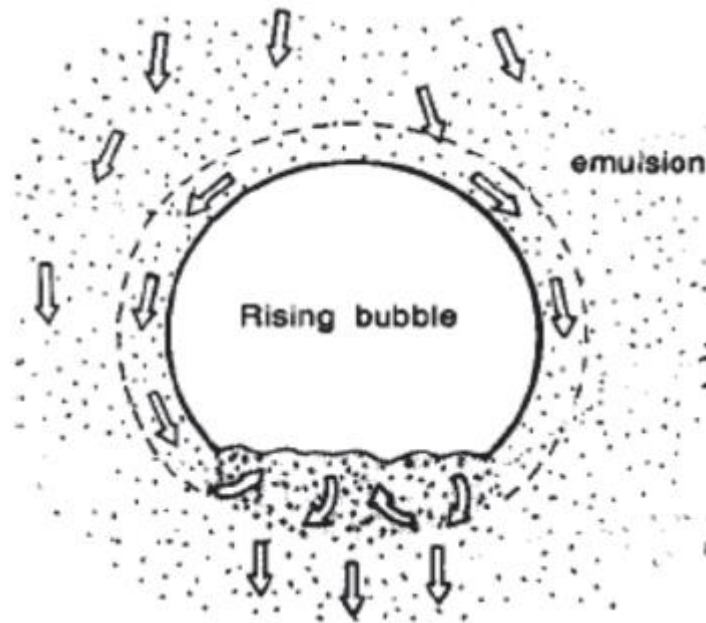


Figure 1.7 Bubble schematic in bubbling fluidized bed [15]

As seen in Figure 1.7, bubbles are nearly hemispherical. The area under the bubble is called the wake, and this area includes an important amount of solid particles. A cloud occurs at the surrounding of the bubbles; this area has solid particles with higher density from inside of bubbles but with lower density than the dense regime.

1.5.2 Geldart's Classic Classification of Particles

Every granular solid particle cannot be fluidized. The motion characteristic of the particle in a fluidized bed mostly depends on particle size and its density. Particles are classified into four main groups by Geldart.

Group A particles can be easily fluidized and generally low gas flow rates are enough for fluidization. Density of this group of particle is not high ($< \sim 1.4 \text{ g/cm}^3$) or/and have a small particle size ($d < 30 \text{ }\mu\text{m}$) [16].

Group B particles are named ‘sandlike’ particles. Generally in this group, particle size changes between 150 μm and 500 μm and the density of particles from 1.4 to 4 g/cm^3 [16]. Glass beads and sand are the best examples of this group.

Group C particles are also called ‘cohesive’ particles. The diameter of the particles usually smaller than 30 μm like group A but fluidization ability is extremely low because of the large interparticle forces. Flour and starch are common examples of this group.

Group D particles are also known as ‘spoutable’ particles. These particles are very dense and diameter also high when compared with other groups. Without an equal flow rate in the bed and an improper bed type, they are not able to fluidize. Coffee beans and lead shots are some examples of this group.

In this experimental study, silica sand will be used as early mentioned. In the Geldart classification, our particles belong to group B.

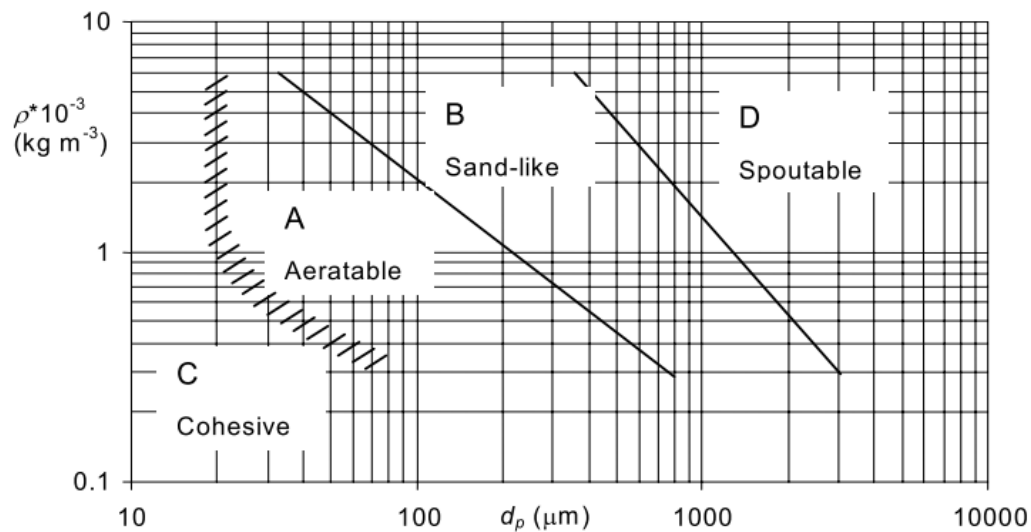


Figure 1.8 Geldart classification of the particles diagram [16]

In fluidized bed applications, if granular particles are not specific, the bed contains particles that have different sizes and shapes. Because of a wide range of particles are not perfectly spherical a term as sphericity (ϕ) is used which defined as the ratio of the surface area of a sphere to the surface of the particle with the same volume. For perfect spherical particles $\phi=1$ but it's less than one for irregular particles. The formulary definition is; [17]

$$\phi = \frac{A_{eq}}{A_p} \quad (3)$$

Here A_{eq} is the perfect sphere surface area and A_p is the surface area of the particle. For nonspherical particles, equivalent diameter term is usable and defined as; [17]

$$d_s = \left(\frac{6V_p}{\pi}\right)^{1/3} \quad (4)$$

In formulation V_p represents particle volume.

With the information of density and diameter, particles are placed in the Geldart's diagram.

1.6 Thesis Overview

In this study, a sand-air fluidized bed was investigated experimentally and simulated with ANSYS Fluent 17.2.

In Chapter 1, the advantages of thermal energy storage systems and how a fluidized bed with granular particles motivated the author was mentioned. Also, milestones about fluidization theory were indicated for basic informing.

In Chapter 2, an experimental study was detailed expressed to the readers with both visually and wordily.

In Chapter 3, model development is briefly mentioned.

In Chapter 4, the results of the experimental studies and simulations were compared and discussed in different aspects.

In Chapter 5, concluding remarks are mentioned in the direction of the results.

CHAPTER 2

EXPERIMENTAL STUDY

In this chapter, the experimental setup will be described in detail and, the eprocedures performed during the experiments will be explained.

The experimental set-up was built at the heat transfer laboratory of the Mechanical Engineering Department of the Middle East Technical University. This laboratory has much equipment such as a furnace, compressors, manometers, thermocouples.

The goal of the experimental study is observing the hydrodynamic and thermodynamic behaviors of a fluidized bed in special cases. Herewith, experiments were performed in two sections;

- 1- Hydrodynamic (cold) experiments
- 2- Thermal (hot) experiments

Section names are directly related to the particle temperature because in cold experiments, particles were used at ambient temperature, but in hot experiments, these were heated up.

2.1 Hydrodynamics Experiments

The experimental setup was ready to perform the experiments after the design, production and necessary modification steps. Hydrodynamics experiments are performed first. The schematics of hydrodynamics experimental set up is shown in Figure 2.1.

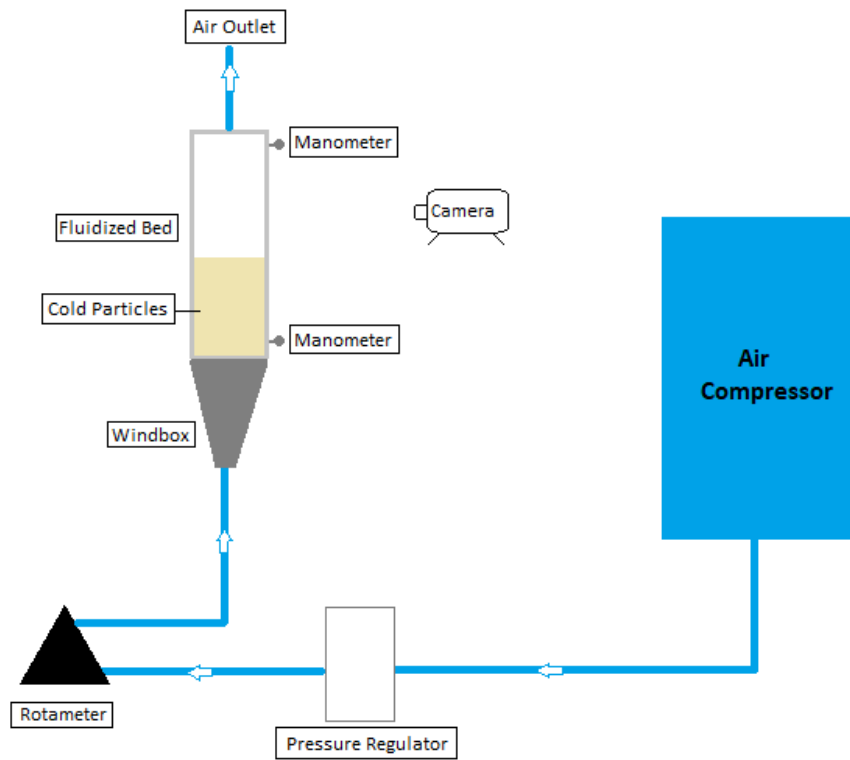


Figure 2.1 Schematics of hydrodynamics experimental setup

The setup consists of an air compressor, bed, wind box, and pipe connections between them; pressure regulator, rotameter, two manometers, camera and granular particles inside the bed.

Figure 2.2 shows the hydrodynamics experimental setup.



Figure 2.2 The hydrodynamics experimental setup

First, the bed and the wind box was designed in the Catia program. These were produced in the machine shop of the Mechanical Engineering Department of the Middle East Technical University. All experiments were carried out in a 0.08 m x 0.4 m x 0.08 m fluidized bed (Fig. 2.3).

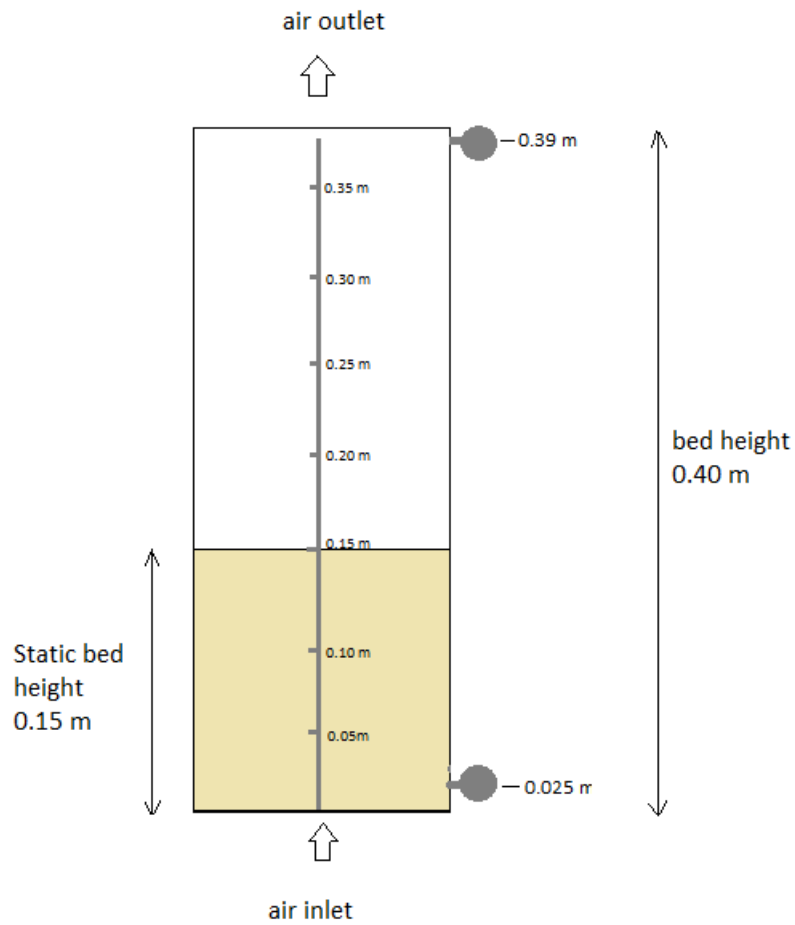


Figure 2.3 Schematic drawing of bed

In cold experiments, the side and back walls were stainless steel and the front wall was plexiglass to observe the motion of granular particles. In hot experiments, all walls were stainless steel with 2 mm thickness because plexiglass is not appropriate for high temperature applications. A conical wind box was produced from the same stainless steel and it was placed between fluidized bed and air pipe to prevent effects of the unbalanced entry of air.

Geldart B type silica sand was used as solid particles with 600-micron diameter and 2300 kg/m^3 density. Fluid was air at ambient conditions in all experiments. Volume fraction of the sand particles was 0.6.

After the experiments with silica sand, hydrodynamics experiments were repeated with CARBOHSP particles. These particles consist of Al_2O_3 , SiO_2 , Fe_2O_3 , TiO_2 and a few more. The density of CARBOHSP is 2500 kg/m^3 and the mean diameter is 350 microns [28].



Figure 2.4 Real view of bed with sand and CARBOHSP particles

Figure 2.4 shows the bed with two different solid particles. At the left side, the bed filled with silica sand particles, at the right side, the bed filled with CARBOHSP particles are shown. For both cases, the static bed height was 0.15 m. CARBOHSP particles were used in hydrodynamics experiments only to compare its behavior with the sand.

During the experiments with sand particles minimum fluidization velocity was measured as 0.252 m/s and minimum fluidization bed height was around 0.165 m.

For the first section of the experiments, two different manometers were placed at 0.025 m and 0.39 m height and middle of the horizontal axis of the sidewall. Manometers were purchased from the Pakkens brand and they can measure pressure between 0-100 millibar. These manometers can be seen in Figure 2.4. During cold experiments, hydrodynamic behaviors like pressure drop and bed expansion of the bed were followed with superficial velocities of 0.38 m/s and 0.46 m/s.

At the bottom and upper of the bed wire meshes were placed to keep particles inside of the bed. During experiments, a common wire mesh was used for CARBOHSP and sand particles. The material of the wire mesh is stainless steel with Cr and Ni. The gap between two wires is 197 micron and wire mesh includes almost 56.000 holes through the bed cross-section. Also, a honeycomb plate was fixed at the bottom of the bed to help the uniform airflow. The seal was applied between bed and wind box for sealing.

A piston compressor was used for air supply, as seen in Figure 2.5. Compressor brand and model are Ozen, TK-300/2x90. It has a 500 lt vessel volume and two cylinders. Its air supply capacity is 700 l/min and system pressure is 8 bars.



Figure 2.5 Air compressor

Between the compressor and fluidized bed, a rotameter and a pressure regulator were fixed on the pipe with 21mm inner diameter to stabilize the air properties. Regulator's brand is Hidroan, AC5010-10-1''.



Figure 2.6 Rotameter and pressure regulator

Two clamps were used to stabilize the vibration of the system. An aluminum folio pipe was used to throw air inside the bed with control.

Experiments were started by activating the compressor to achieve its maximum system pressure. When oscillations on manometers decrease pressures were recorded with the help of a camera. The necessary flow rate value was calculated from multiplying the desired inlet velocity and the cross-sectional area of the bed. During all experiments, the flowmeter was observed to prevent the compressor's sudden air supply inside through the bed from the inlet position. One or two adjustments were made by hand to stabilize the airflow rate during the experiments. Pressure values and motion of sand particles were recorded in every two minutes. Pressure results were obtained by the processing of videos. During processing, three different values were saved in a second and these values were averaged to obtain a result for each superficial velocity. Pressure drop experiments were repeated with superficial velocities of 0.21 m/s, 0.38 m/s, 0.46 m/s, 0.52 m/s and 0.6 m/s.

2.2 Thermal Experiments

Thermal (hot) experiments are the second section of this study. This second setup was constructed by changing hydrodynamics experimental setup. The main difference was the temperature of the particles. K type thermocouples were inserted into the center of the bed vertically at seven different elevations on a thin tube. The test setup was prepared for higher temperatures, but higher temperatures could not be obtained due to the limitation of the furnace. The tube was used to keep thermocouple places fixed. The ceramic blanket insulator was used on the outside of the bed with 0.1 W/mK thermal conductivity and 1000 J/kg-K capacity of specific heat. The thickness of the insulator was 10 cm. Keysight-34972A model data logger was used during all experiments.

Before starting the thermal experiments, sand and CARBOHSP particles were heated in the furnace shown in Figure 2.7. A stainless steel container was designed and produced compatible with the furnace's inner dimensions to insert the particles into the furnace. Heated particles were poured in the bed by hand. As in the hydrodynamics experiments, the compressor was activated before starting experiment. The same superficial velocities were applied to the bed and the temperatures of 7 different points were recorded with the data logger.



Figure 2.7 Furnace

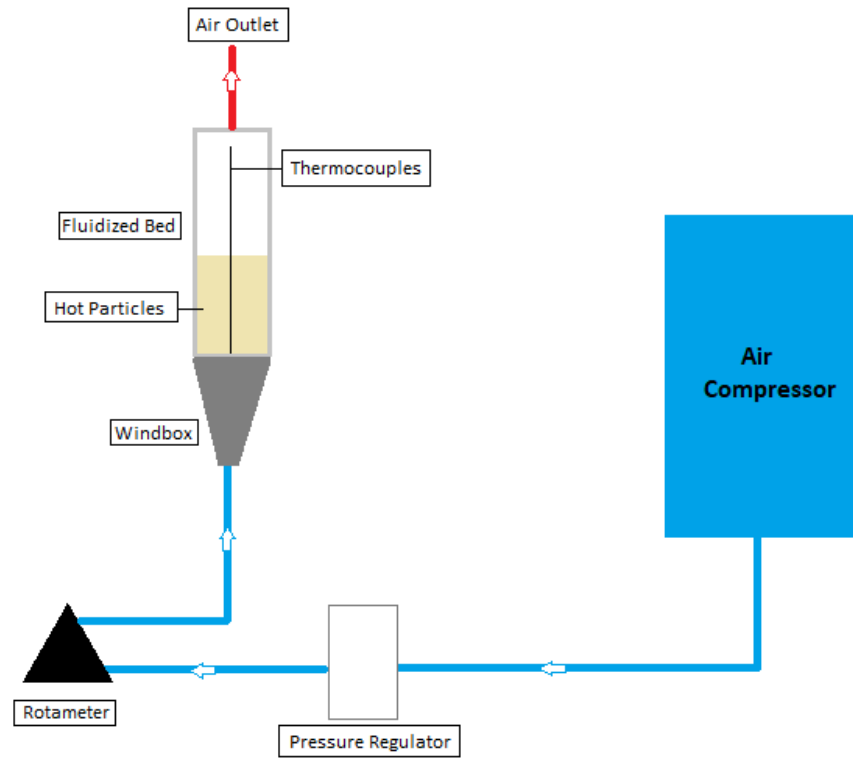


Figure 2.8 Schematic of thermal experimental setup

Figure 2.9 shows the thermal experimental set-up. The insulation material, the thermocouples and the data logger are the differences from the first set-up.



Figure 2.9 The thermal experimental set-up

During the experiments, few factors were observed which affected the accuracy of the experimental results. The major factor is the fluctuations in the manometers and flowmeter. During the pressure drop measurements, manometers were continuously oscillated, and average pressure was determined by the data from the video via the eyeball method. Flowmeter was also slightly oscillated, and this caused to fluctuations in the superficial velocity. Also, while determining the bed expansion

level eyeball method was used and this caused some deviations. Bubbles inside the bed and vibration due to the compressor are the other reasons for the fluctuations.

2.3 Expected Uncertainty

During experimental studies, there is a difference between the true value and measured value, which named as the error. Uncertainty term can be explained as the possible error value in measurements. Uncertainty can be originated from several reasons: measuring system errors, system-sensor interaction errors, system disturbance errors, etc. Analyzing the uncertainty helps to understand the effects of these errors on measurements. There are two types of uncertainties: single sample and multiple sample ones. The difference is related to many taken independent data from different test points [18]. In this study thermocouple-data logger system records only one data in per two seconds so it can be categorized as a single sample experiment.

In heat transfer experiments, velocity, radiation and conduction problems on the probe are examples of possible error sources. In standard K-type thermocouples, expected uncertainty is given as $\pm 2.2\text{ C}^\circ$. This range can be reduced to $\pm 1.1\text{ C}^\circ$ in special types.

In the spec sheet of data acquisition system this range is indicated as $\pm 2.1\text{ C}^\circ$ and this value is equal to the sum of the probe accuracy ($\pm 1\text{ C}^\circ$) and probe vendor specified accuracy ($\pm 1.1\text{ C}^\circ$).

Reasons for the errors (fluctuations, eyeball method) in hydrodynamic experiments are stronger than the expected uncertainty, thus the manometers are left out of expected uncertainty analysis.

CHAPTER 3

CFD MODEL DEVELOPMENT

Hydrodynamics and thermal experiments were the first part of this study. After completing measurements, the fluidized bed was modeled for hot and cold particle cases. In this chapter, the numerical model of fluidized bed is explained.

3.1 Physical Components of the CFD Model

In this study; solid particles, fluidizing gas, and bed geometry creates the essential physical components of the system.

3.1.1 Solid Particles

In fluidized bed studies, various solid particles were investigated as solid phase. Diameter, specific heat capacity, chemical composition, conductivity, and porosity are some important properties for selecting the particles. If the particles will be used in a large system, the cost is also an important parameter. As mentioned in the experimental setup section, amorphous silica sand was used in the fluidized bed system. There are many motivations to select sand in dense fluidization regimes;

- Thermally stable at high temperatures (+900 °C) and this directly affects cycle efficiency,
- Low cost and availability,
- Non-toxic, non-flammable,

- Act as both heat transfer surface and storage medium so no need for a costly heat exchanger.

The thermal properties of sand generally tend to be in linear variation with temperature. At room temperature, the specific heat capacity of the sand particles is around 920 J/kg K and it is nearly 1130 J/kg K at 1000 K. Again at room temperature, the thermal conductivity is 1 W/mK and almost 2 W/mK at 1000 K [19][29]. As mentioned before, silica sand belongs to the Geldart B type particle group.

In this study, CARBOHSP particles are investigated only experimentally because the necessary information for simulations could not be found.

3.1.2 Fluidization Gas

In fluidized bed systems, liquid or gas materials are used as fluid. Water can be a good example of the liquid type. CO₂ and air are the commonly used fluids in gas phase. When gas type fluids are used in fluidized bed system moisture level becomes an important parameter because it directly affects the quality of fluidization due to moisture may make particles sticky. Air is determined as fluid in this study because it is a good choice for fluidization, easy to use and no cost.

3.1.3 Bed Geometry

In the literature, different sizes and shapes of bed geometry were tested, but the most preferred geometries are cylinder and the rectangular prism. Taghipour et al. [20] were used a 0.28x1 m rectangular 2D system, Syamlal et al. [21] were used an axisymmetric 2D geometry with H=2 m and D=0.229 m and Peirano et al. [22] were used a rectangular 3D system with dimensions of 0.8x0.7x0.12 m.

In this study, all experiments and simulations were occurred in a bed with dimensions 0.08 m width, 0.08 m depth and 0.4m height. Rectangular prism bed shape has an advantage for minimizing the total area for multi-bed designs. User-defined design parameters are shown in Table 1.

Table 1. Parameters of physical model

Bed height	0.4	m
Bed width	0.08	m
Bed depth	0.08	m
Static bed height	0.15	m
Particle density	2300	kg/m ³
Air density	1.225	kg/m ³
Mean particle diameter	600	μm
Initial void fraction	0.6	-
Superficial air velocity	0.38 , 0.46	m/s
Temperature of air inlet	300	K
Temperature of initial sand particles	585	K

3.2 Solution Approach

The structure of fluidized bed consists of two different phases as gas and solid so CFD model built with the aid of multiphase flow and Eulerian-Eulerian model in ANSYS Fluent 17.2. All simulations were solved with pressure-based solver and as transient. Gravity was defined as 9.81 m/s².

In the Eulerian-Eulerian approach, mass balance, momentum balance, and energy balance equations are derived separately for each phase. These balances are correlated with volume fractions of the phases. The conservation of the mass can be expressed as;

$$\frac{\partial}{\partial t}(\epsilon_m \rho_m) + \nabla \cdot (\epsilon_m \rho_m \vec{u}_m) = 0 \quad (5)$$

Because there is no mass change and mass transfer between phases in this study, the right-hand side of the formula is zero. On the left-hand side, the first term represents the mass accumulation and the second term is the mass flux rate. Momentum balance equations for gas and solid phases can be expressed as [20];

$$\frac{\partial}{\partial t}(\epsilon_g \rho_g \vec{u}_g) + \nabla \cdot (\epsilon_g \rho_g \vec{u}_g \vec{u}_g) = -\epsilon_g \nabla P + \nabla \cdot \bar{\bar{\tau}}_g + \epsilon_g \rho_g \vec{g} + K_{gs}(\vec{u}_g - \vec{u}_s) \quad (6)$$

where s and g represent the solid and gas phases. K_{gs} is the momentum exchange coefficient between gas and solids. P is pressure and $\bar{\bar{\tau}}_g$ is stress tensor for the above equation. The first term is momentum change, and the second term is momentum transfer on the left-hand side. Equation (7) shows the energy balance equation of the phases.

$$\frac{\partial}{\partial t}(\epsilon_m \rho_m h_m) + \nabla \cdot (\epsilon_m \rho_m \vec{u}_m h_m) = \epsilon_m \frac{\partial P_q}{\partial t} \nabla + \bar{\bar{\tau}}_m : \nabla \vec{u}_m - \nabla q_m + Q_{int} \quad (7)$$

On the right hand side, the terms represent flow work, heat production because of the viscous dissipation, the heat flux of convection and heat exchange of solid and gas phases in line.

The most significant transfer mechanism between phases is drag forces in fluidized beds. Syamlal and O'Brien drag correlation was applied for the drag model [19][29]. Due to the cellular structure of dense regime, particle-particle collisions occur and, it leads the momentum transfer between particles. The stress that occurs from the collisions is named collisional stress. Restitution coefficient (e_{SS}) is a term that defines this particle collision's elasticity. If $e_{SS}=1$ this means fully elastic collisions otherwise collisions are inelastic. In this simulation restitution coefficient is assumed to be 0.99.

Frictional stress is another type of stress on particles in dense regimes due to contact of particles to each other. Frictional viscosity was derived from frictional stress calculations by Johnson and Jackson [19] and this model was assumed in simulation.

In the dense regime, granular particles tend to keep together due to the bulk viscosity of solid phase. The bulk viscosity definition by Lun et al. is taken into consideration in that simulation [19].

While validating the gas-solid fluidized bed's experimental results with the CFD model, some coefficients are used for accurate comparison. Restitution coefficient and specular coefficient are very important parameters while modeling the interactions between particle-wall and particles each other. Restitution coefficient directly affects the pressure fluctuations, size of the bubble, and rising velocity. In the study of Hicdurmaz [19][29], several restitution coefficients and specular coefficients were tabulated for an averaged void profile to find the best option. As a result, the restitution coefficient was selected 0.99 as early mentioned and the specular coefficient was determined as 0.1.

As the numerical solution approach, phase coupled SIMPLE algorithm was selected due to suitability for pressure-velocity coupling.

In hydrodynamics simulations, pressure drop across the bed and the bed height variation were converted.

The above approaches are common to both hydrodynamics and thermal simulations. For the thermal model, some other settings and approaches were applied. Firstly, thermal properties of air and sand are not constant due to temperature change with time so these were set as temperature dependent by piecewise-linear method. Heat loss from the walls by convection was considered in boundary conditions with the shell method. The thermal conductivity and thicknesses of stainless steel and insulation materials are the key parameters in this method.

Also, the heat transfer coefficient of air was set as 5 W/m²K due to the natural convection considered during heat loss to the ambient. Figure 3.1 illustrates the heat loss process, on the left-hand side of the figure represents the inside of the bed. The deficiency of this setting is that thermal contact resistance was ignored because its accurate prediction is very hard.

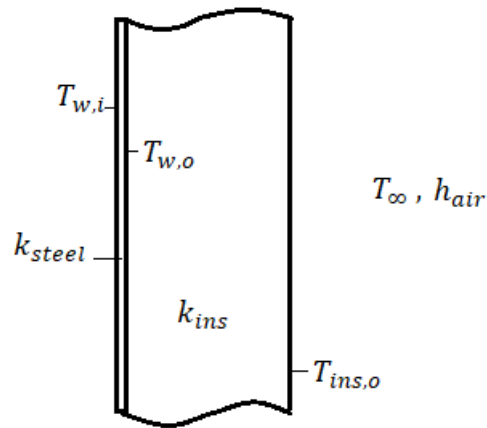


Figure 3.1 Heat loss points through the outside of the bed

Heat transfer mechanism between phases is very important for fluidized bed modeling and it can be detailed as;

$$Q_{int} = hA(T_s - T_g) \quad (8)$$

where h is heat transfer coefficient between gas and solid. Temperature and interphase heat transfer coefficient (h) is the parameters that are obtained from the thermal model simulations. Gunn [23] Nusselt number correlation was considered for thermal interphase interactions.

$$Nu_s = (7 - 10\varepsilon_s + 5\varepsilon_s^2)(1 + 0.7Re_s^{0.2}Pr^{1/3}) + (1.33 - 2.4\varepsilon_s + 1.2\varepsilon_s^2)Re_s^{0.7}Pr^{1/3} \quad (9)$$

Here Pr is the Prandtl number and Re_s represents the Reynolds number for particles and it is defined as

$$Re_s = \frac{\rho_s d_s |\vec{v}_s - \vec{v}_g|}{\mu_g} \quad (10)$$

s and g subscripts represent the solid and gas phases.

Interphase heat transfer coefficient can be yield from below relation

$$Nu_s = \frac{h d_s}{k_g} \quad (11)$$

where k_g defines the conductivity of air.

All these correlations were set as user-defined functions to calculate the interphase heat transfer coefficient.

3.2.1 Mesh Refinement Study

Cubic meshes are created uniformly by ANSYS Meshing tool. If the diameter of the particle is higher than the ten times of the mesh size accuracy of the results is exceedingly high [30]. Also, acceptable results are achieved by higher ratios than the ten in the literature. [7]. Figure 3.2 shows the meshed domain of the simulation study with 5 mm mesh size.

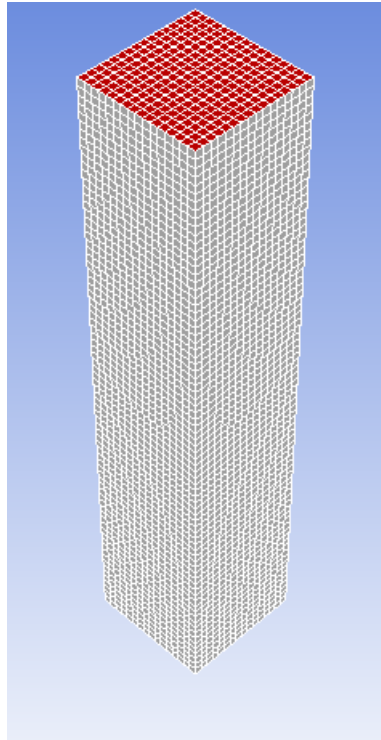


Figure 3.2 Mesh setting for computational domain

The ratio between particle diameter and mesh size is enough for satisfying results, but a relative study is required for grid independence. Therefore, 2.5 mm x 2.5 mm mesh size is selected to compare the results. Figure 3.3 shows bed height variation with time at different mesh sizes. Change leaning of the graph shows that an important deviation does not exist between the bed heights of different meshes. Because of finer meshes leading to higher computational costs and results are close enough 5 mm x 5 mm mesh size is selected during the simulations.

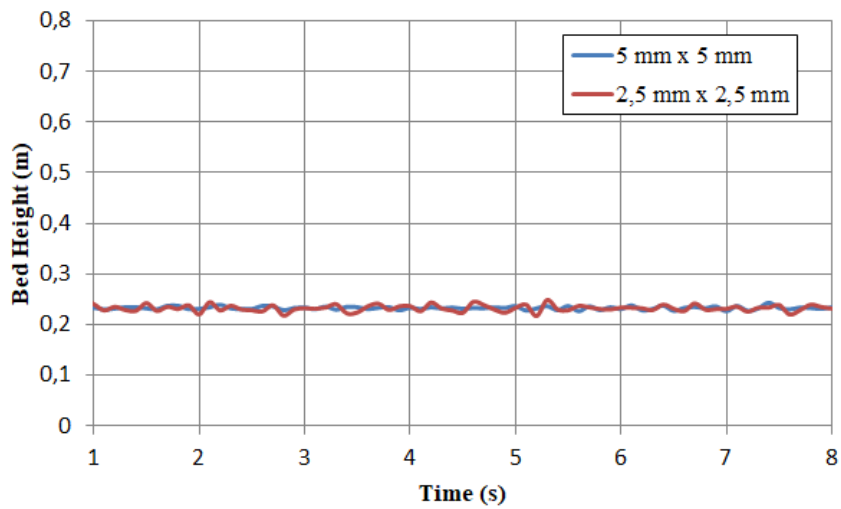


Figure 3.3 Temporal bed heights for various mesh sizes

3.2.2 Time Step Optimization

The most important parameters of the time step size selection are computational costs and convergence during the solution. Different time step sizes should be tested to get the best results.

In this study, $1e-3$ s, $5e-4$ s and $1e-4$ s time step sizes are compared. Figure 3.4 shows pressure drop variation with different time step sizes. $1e-3$ s was accepted for best choice because average value of the different time step sizes is extremely close. Real experiment results are compatible with the numerical results so that time step size was chosen with a maximum iteration number as 20 for lower computational costs.

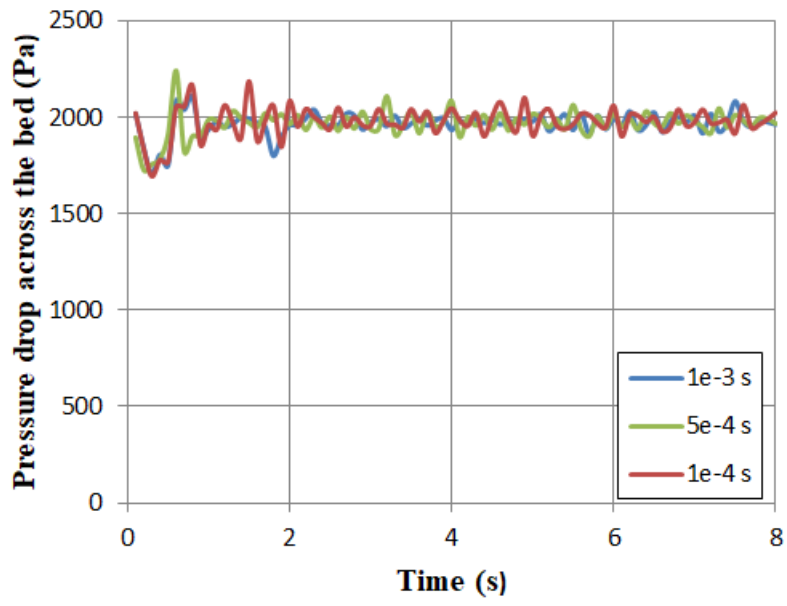


Figure 3.4 Temporal pressure drop variation for different time steps

CHAPTER 4

RESULTS AND DISCUSSION

Experimental and CFD model studies were introduced separately in previous chapters. Results of simulations were validated with experiments to define real-life results as accurate and repeatable. In this chapter, the results were compared and discussed.

4.1 Hydrodynamics Results

In gas-solid fluidized bed applications, many hydrodynamical properties can be discussed. Pressure drop, voidage profiles, velocity distribution of granular particles, inconstant bed height levels and, shape of bubbles are the significant parameters in hydrodynamic verification. In this study, pressure drop and bed height were dealt with due to their computational characteristics [19][29].

4.1.1 Pressure Drop

Change of pressure drop in a specific region of the fluidized bed diagram is one of the best expressions in the hydrodynamic field. In theory, pressure drop linearly changes with velocity increase until minimum fluidization conditions and then stays constant at higher superficial velocities. Theoretical change diagram is shown in Figure 4.1.

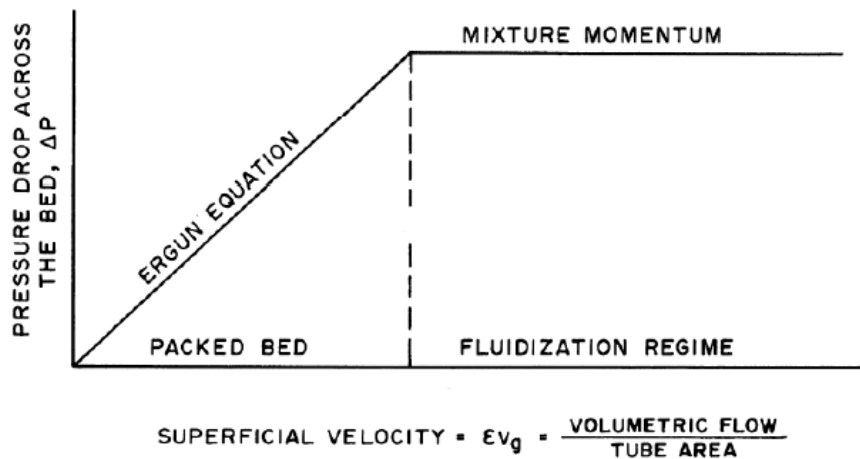


Figure 4.1 Theoretical change of pressure drop with superficial velocity [24]

In reality, the diagram is slightly different from theoretical diagram as shown in Figure 4.2. Pressure drop changes linearly at low flow rates similar to theory. After reaching the maximum pressure drop a small amount of decrease is observed and this stationary pressure condition is named as static pressure of the bed. This decrease can be explained by the change in voidage. At that point, void fraction increases from the fixed bed condition to the fluidization condition. After this decrease, pressure drop remains stable instead of the gas velocity rise. When superficial velocity starts to diminish void fraction returns to the initial fixed bed value from the fluidization value, and this passing occurs gently without any sudden changes.

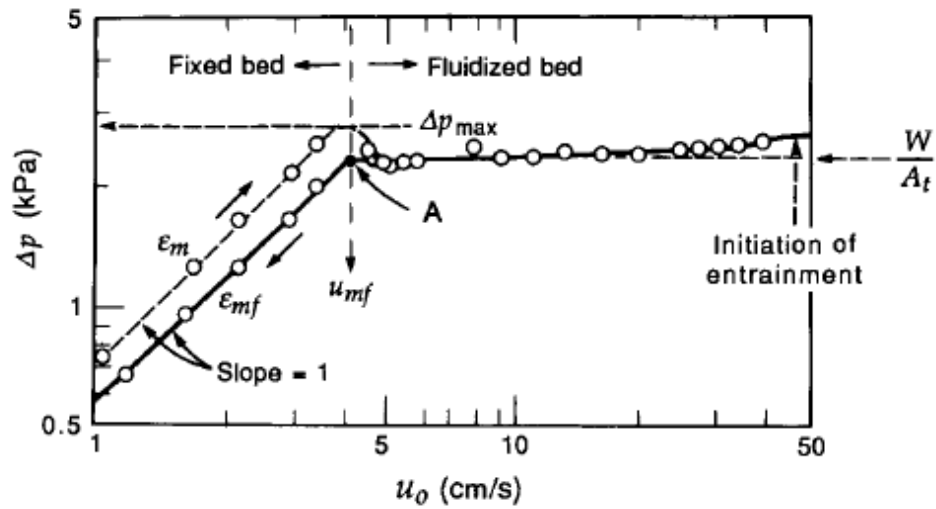


Figure 4.2 Pressure drop across the bed change with superficial gas velocity [14]

This stationary behavior of the pressure drop can be explained from the definition of static pressure inside the bed. If wall interaction is ignored, static pressure drop can be defined as the total weight of particles divided by the cross-section area of the bed and this explanation is independent of the gas velocity.

Figure 4.3 shows experimental results of this study and Taghipour's [19][20]. Pressure drop across the bed values were compared at 0.21 m/s, 0.38 m/s and 0.46 m/s superficial velocities. The tendency of results is stable similarly with theory. Numerical values of the results are not the same due to different bed geometries. As mentioned before weight of the particles and cross-sectional area directly affects the pressure drop and both of them are different for these cases.

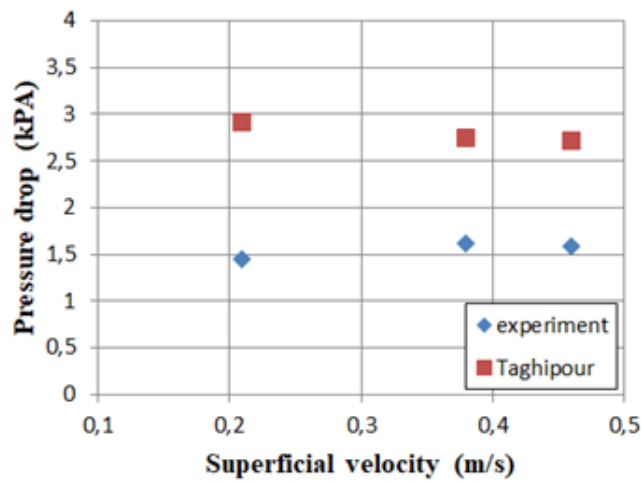


Figure 4.3 Pressure drop inside the bed at different experimental studies

In literature, pressure drop change was studied with different drag models. Syamlal O'Brien model more accurately foresees the pressure drop pattern [19][29]. Figure 4.4 shows experimental and CFD results of pressure drop across the bed. Pressure drop values tend to be almost constant at both results as predicted.

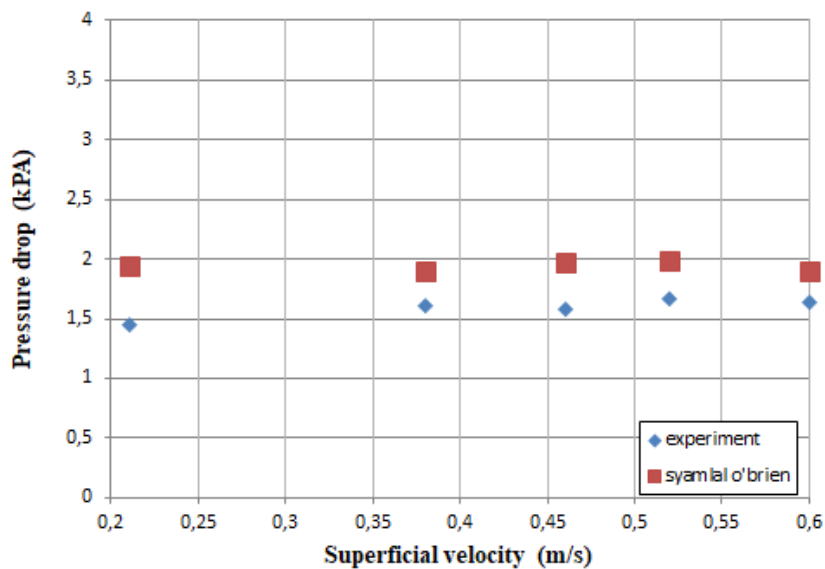


Figure 4.4 Pressure drop inside the bed ($P_{y=0,025 m} - P_{y=0,39 m}$)

Hydrodynamics experiments were repeated for CARBOHSP particles after sand. The aim of these measurements was to observe the behavior of new particles and discussing the effects of different parameters. In Table 2, important velocities of different particles are compared. In theoretical calculation, minimum fluidization velocities of sand and CARBOHSP particles are found as 0.236 m/s and 0.071 m/s from equation (1). Additionally, terminal velocities are found as 4.521 m/s and 2.393 m/s from equation (2). Minimum fluidization velocity of sand is higher than CARBOHSP particle and reason behind this value may relate with higher sphericity and small diameter of CARBOHSP particles.

Table 2. Important velocities of different particles

	SAND	CARBOHSP	
minimum fluidization velocity	0.252	0.174	m/s
minimum bubbling velocity	0.338	0.260	m/s
terminal velocity	2.611	1.988	m/s

As seen in Figure 4.5, pressure drop across the bed with CARBOHSP particles is higher than the pressure drop with sand at the same superficial gas velocities. As explained before, the reason is related to basic pressure definition. In the same volume, the weight of CARBOHSP particles is higher than the weight of sand the particles. Bed cross-section area is same for both cases so pressure drop is higher at fluidization bed with CARBOHSP particles.

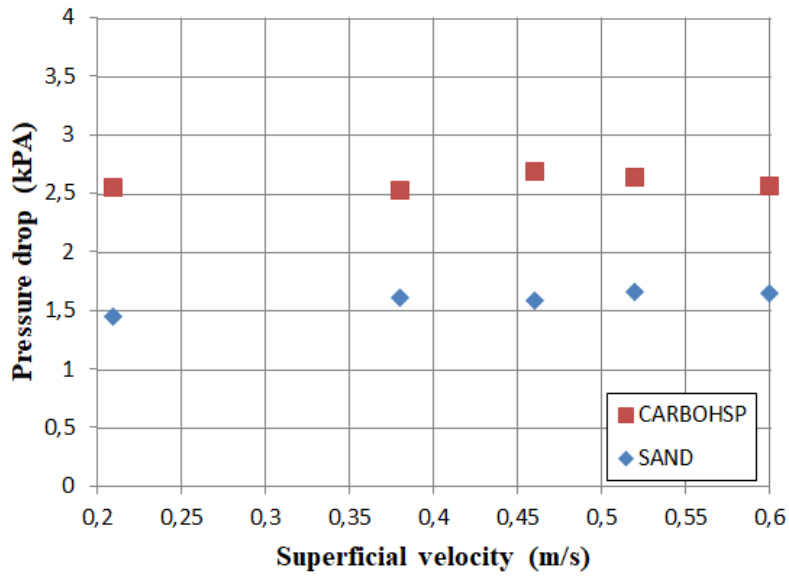


Figure 4.5 Experimental pressure drop variation with different granular particles
 ($P_{y=0,025\text{ m}} - P_{y=0,39\text{ m}}$)

4.1.2 Bed Expansion Ratio

Bed expansion is a natural result in two-phase fluidized bed systems. Bed expansion is affected by the two factors, the dense phase's expansion degree and bubbles [25]. After the minimum fluidization point, increasing the superficial velocity causes the bubbling linearly and bed expansion occurs due to space occupied by the gas bubbles.

The bed expansion ratio can be explained as bed expansion divided by the initial bed height.

$$\% \text{ Bed Expansion Ratio} = \left(\frac{H - H_0}{H_0} \right) * 100 \quad (12)$$

In Figure 4.6 experimental and simulative bed expansion changes analyzed by the eyeball method. As expected bed expansion ratio rises with superficial velocity rate.

The reason for the difference between the experimental and simulation results originated from the drag model. Syamlal O'Brien drag model couldn't envisage the fluidization at low velocities [19][29].

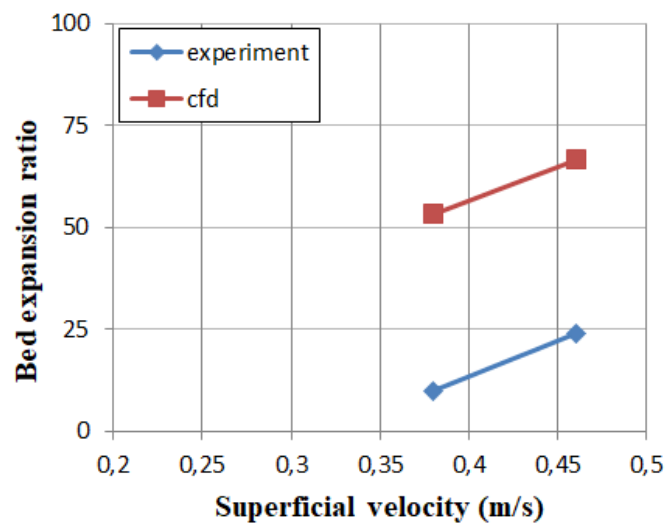


Figure 4.6 Experimental and simulated bed expansion ratio of sand particles for different velocities

The bed expansion ratio is one of the best metering tools for comparing the hydrodynamic behaviors of particles. As mentioned in pressure drop section, CARBOHSP particles were tested to observe differences between sand particles. Figure 4.6 was created to see the bed expansion ratio trend of CARBOHSP particles.

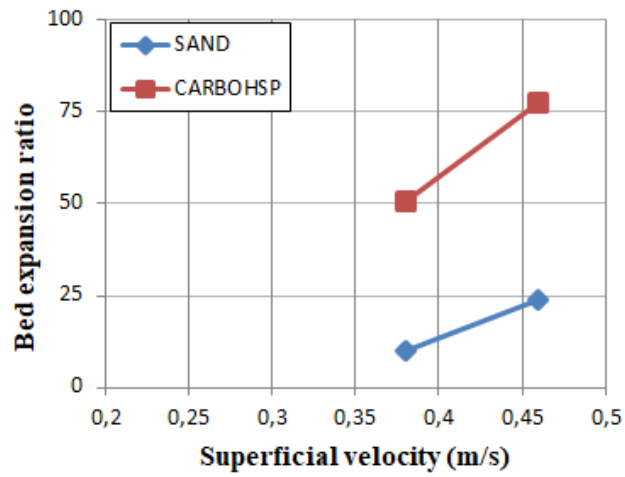


Figure 4.7 Experimental bed expansion ratios of sand and CARBOHSP particles

As seen in Figure 4.7, CARBOHSP particles have a higher bed expansion ratio than sand particles at the same superficial velocities. Smaller diameter and higher sphericity of CARBOHSP particles are the main reasons of this difference [26].

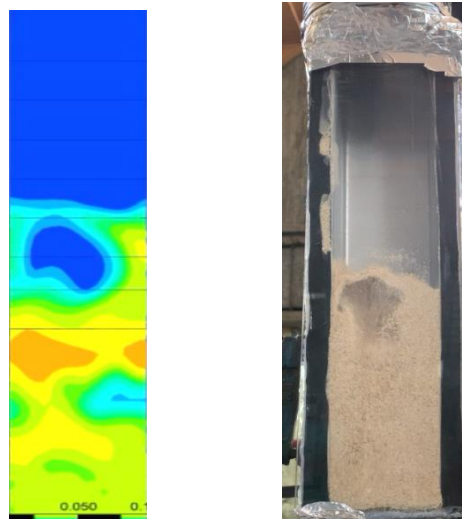


Figure 4.8 Similar views of bubbles in experimental and CFD studies

Figure 4.8 shows similar extended beds and bubble shapes from the experiment and simulation scenes at the same superficial velocity $u=0.38$ m/s.

4.2 Thermal Results

As mentioned before, the most important advantages of the fluidized bed is the capability of heat storage and achieving the hot air from hot granules. To observe the thermodynamic behavior of this model, the temperature and interphase heat transfer coefficient between phases were considered.

4.2.1 Temperature Gradient

The temperature gradient was obtained with the help of K-type thermocouples and CFD simulations separately. Initial temperatures of air and sand were measured nearly 300K and 585 K respectively in experiments also these temperatures were set in simulations as initial values. Temperature of the air comes up to sand temperature in 0.03 s inside the static bed elevations. This short time refers to that air-particle resistance is very small during the convective heat transformation. Figure 4.9 shows the temperature gradient of sand particles and air. The reason for not straight distribution is bubbling regime in the fluidized bed and same figure concludes that both phases have almost the same temperature during the process.

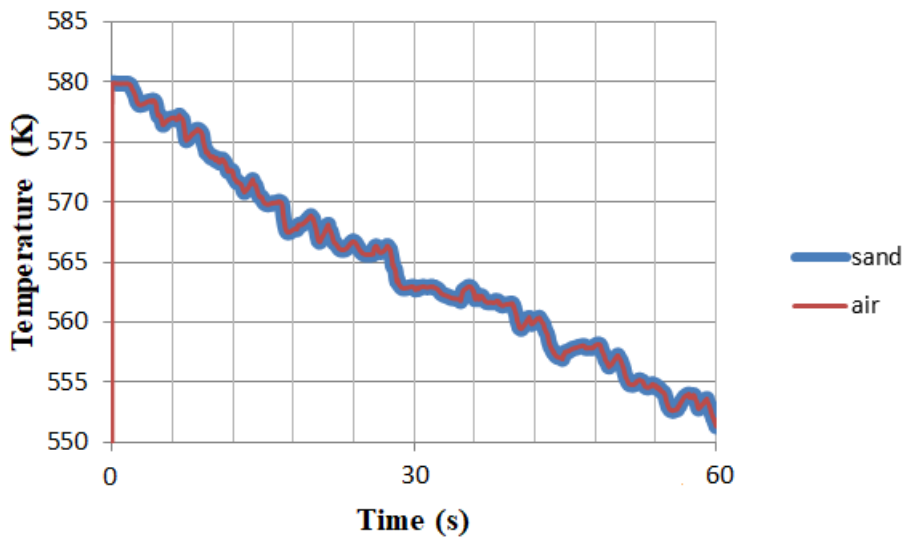


Figure 4.9 Temperature variations of phases at first 60 s in CFD results at $y=0.10$ m and $u=0.38$ m/s

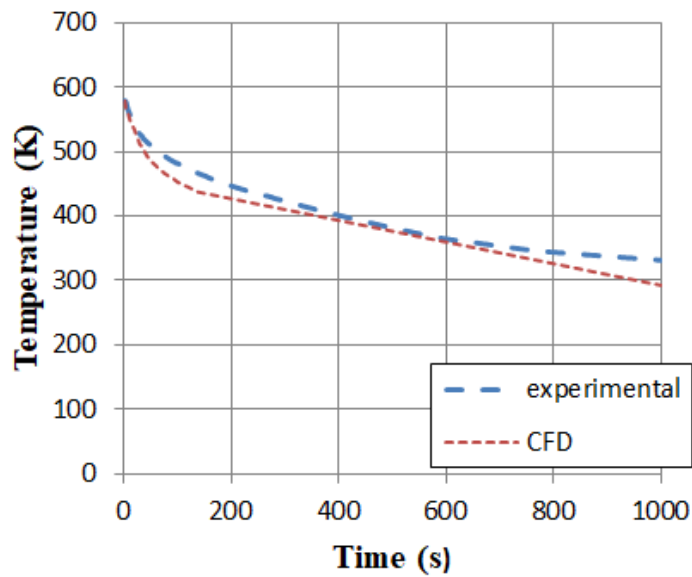


Figure 4.10 Air temperature variations of experimental and CFD results at $u=0.46$ m/s and $y=0.10$ m

Figure 4.10 shows how temperature gradient changes with time in experiment and CFD simulation under the same conditions. Results belong to temperatures at $y=0.10$ m while superficial velocity is 0.46 m/s, and the model was simulated for the first 1000 s. The most compatible results were obtained from when the elevation was 0.10 m as expected. This location is the center of the initial sand mass and outermost point to the high fluctuation levels. Lower temperature attitude of CFD analysis can be explained with the high heat loss due to the ignoring of the thermal contact resistance.

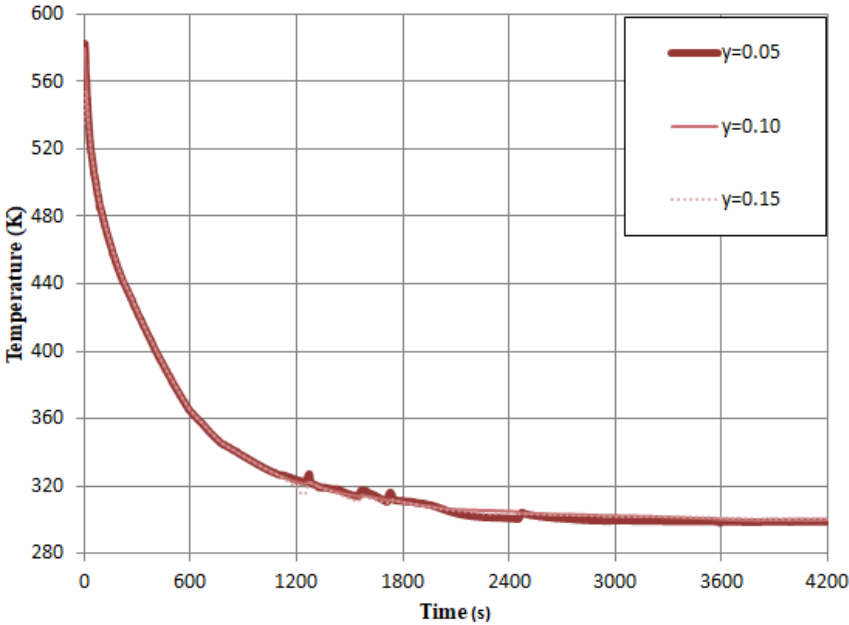


Figure 4.11 Experimental air temperature values at different elevations, $u=0.46$ m/s

During the experiments, temperature is measured from different points of the bed. Figure 4.11 indicates the trend of temperature changes at various elevations when $u=0.46$ m/s. When the height of the measurement point increases initial temperature of that point decreases. Main reason for this variety is after furnace process sand

was spilling into the bed manually and a time difference occurred. Notwithstanding this, after a short time, all points show almost the same temperature gradient because of the bulk acting of sand particles. Also, some peaks are observed on the temperature gradient due to the bubbling regime in the bed.

Additionally, bed temperature comes to initial room temperature after 4200 s when $u=0.38$ m/s. It means heat storage system supplies 70 minutes of hot air after the heat source is deactivated.

After completed the thermal experiments with sand particles, procedure was repeated by CARBOHSP particles to see the distinction between solids. Figure 4.12 shows how those particles getting cooler at same superficial velocity. This figure indicates that sand and CARBOHSP particles show similar trends in the cooling process.

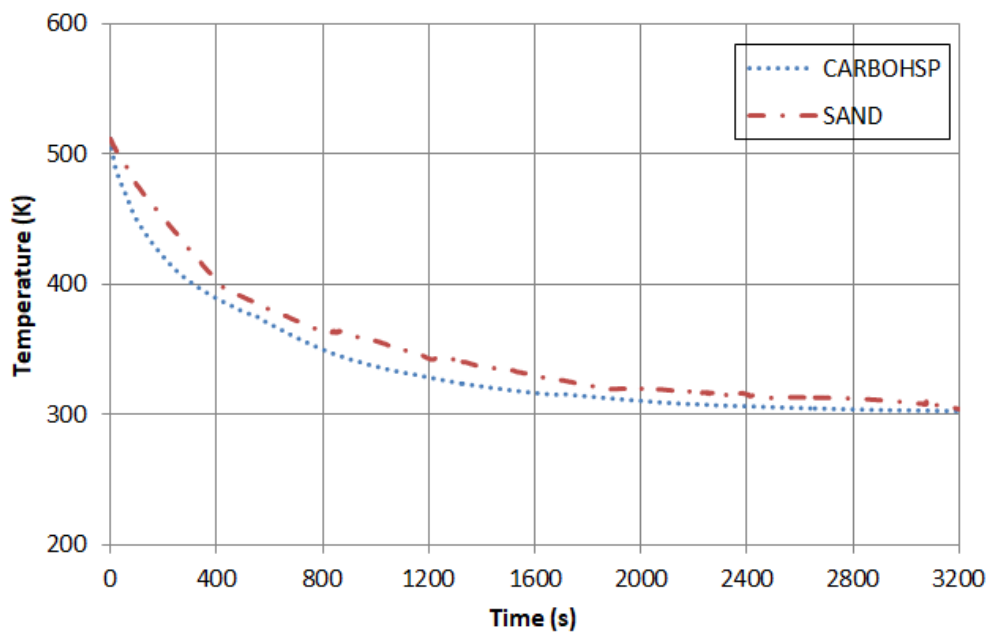


Figure 4.12 Experimental air temperature variations of fluidized bed with sand and CARBOHSP particles when $u=0.38$ m/s and $y=0.10$ m

4.2.2 Heat Transfer Coefficient Between Phases

The solution approach of interphase heat transfer coefficient was stated in the previous chapter. Equation (11) shows that; interphase heat transfer coefficient is the function of air thermal conductivity and Nusselt number. Gunn's Nusselt number correlation explains that Re_s , Pr and sand volume fraction affects the heat transfer coefficient. If details of Re_s and Pr numbers are considered, weakness of connection between temperature is easily realized. It means that the overwhelming factor on the heat transfer coefficient is air thermal conductivity. Air thermal conductivity increases by temperature. It explains why the heat transfer coefficient decreases by the drop in bed temperature. In the simulation, heat transfer coefficient was calculated from different heights and with different velocities.

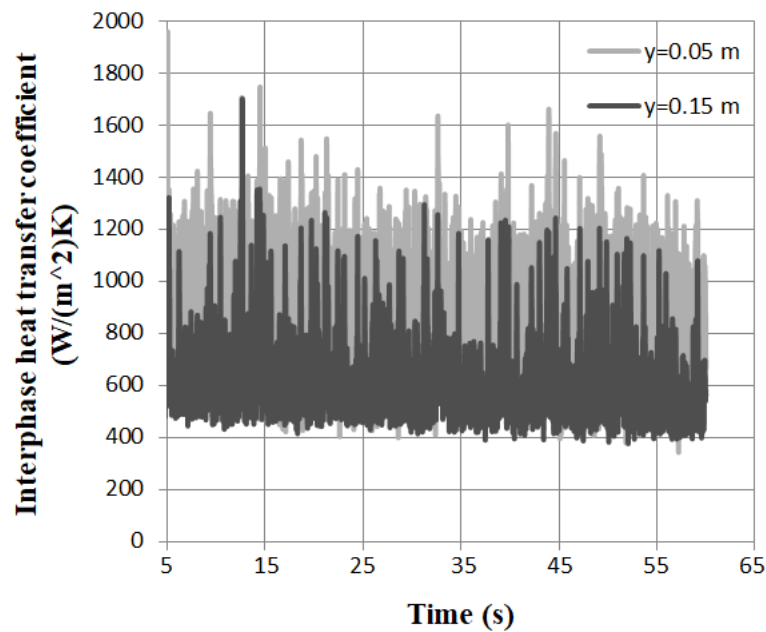


Figure 4.13 Real attitude of interphase heat transfer coefficient ($u=0.38\text{m/s}$)

In Figure 4.13, the real alteration of interphase heat transfer coefficient is shown. These fluctuations occur due to the bubbles. As known, solid volume fraction directly affects the h and the bubbling regime continuously changes this ratio, and therefore linear changes could not be observed. The next figure for the heat transfer coefficient includes mean values of every 5 seconds to see more clear diagrams.

In Figure 4.14, heat transfer coefficient values are plotted at various elevations. Simulation was repeated with superficial velocities of 0.38 m/s and 0.46 m/s. As seen in the figure, the heat transfer coefficient is changed by elevation oppositely. The solid volume fraction may be the main reason for this decrement. Equation (9) states that when ϵ_s increases Nu and interphase heat transfer coefficient decrease.

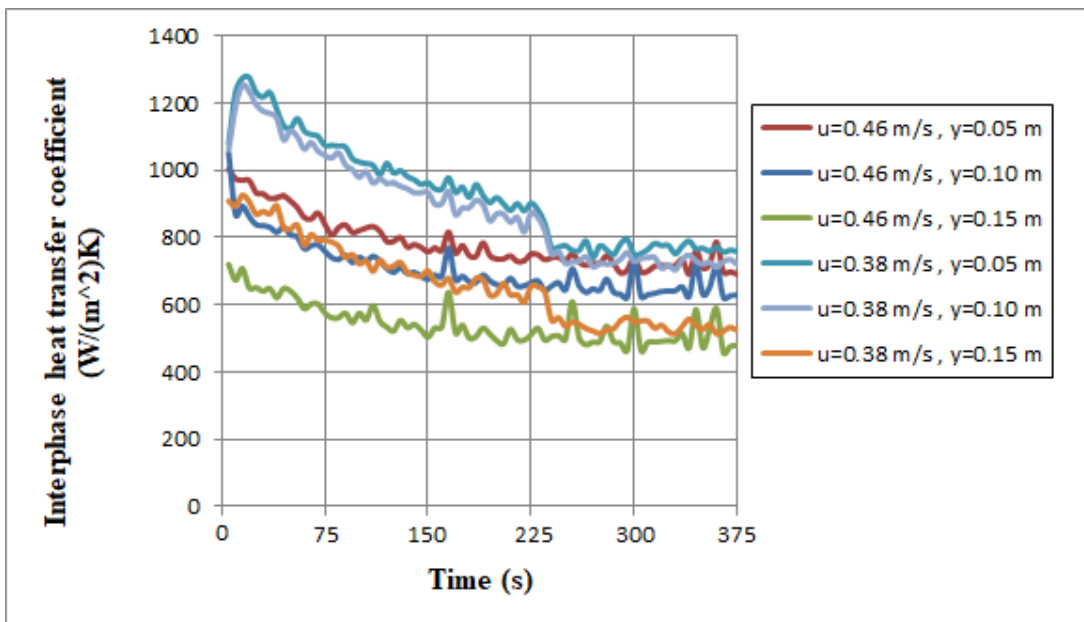


Figure 4.14 Interphase heat transfer coefficient change with time from CFD results at different elevations

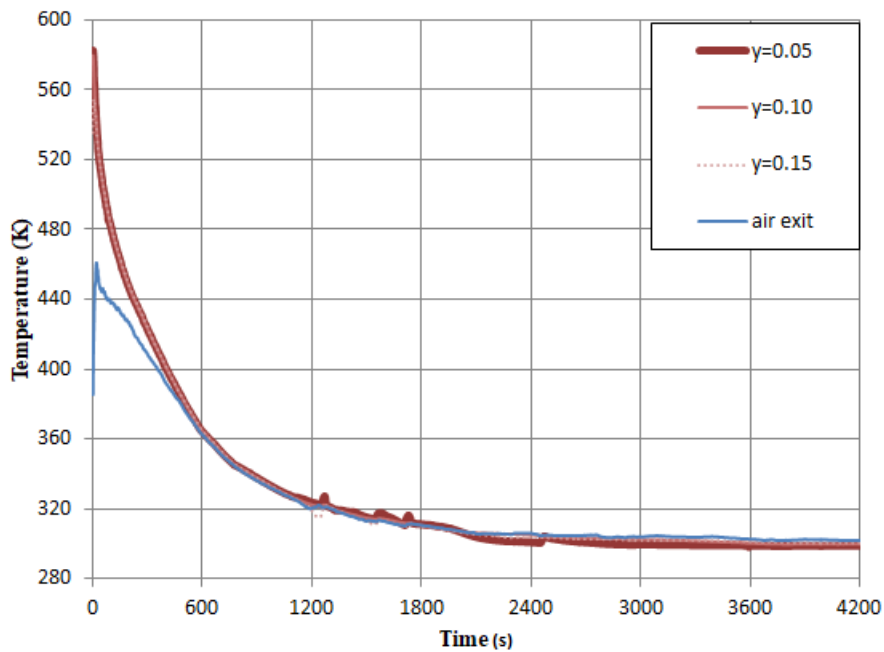


Figure 4.15 Experimental variation of the air exit temperature at $u=0.46$ m/s

Figure 4.15 shows how the temperature of exit air changes with time. This temperature variation of phases differs from the results of Hicdurmaz's study. In his study, after a very short time, different phase temperatures were equal. The main reasons for this difference may be using different bed geometry and heat loss due to not perfect isolation.

4.2.3 Heat Transfer Analysis Between Phases

In previous pages, the results show similar trends between phases and validation methods. Last, a heat transfer analysis is necessary to display the efficiency of the system.

In fluidized bed systems, three basic heat transfer mechanisms are still valid. These are conduction between particles, conduction between particles and walls, convection between particles and fluid, and radiation. General energy balance can

be written as

$$m_s c_{p,s} \frac{dT}{dt} = Q_{s-s} + Q_{s-f} + Q_{rad} + Q_{s-wall} \quad (13)$$

Here, m_s represents the mass of sand, $c_{p,s}$ is specific heat capacity of sand particles, Q_{s-s} is solid-solid conduction, Q_{s-f} is solid-fluid convection, Q_{s-wall} is solid-wall conduction, and Q_{rad} is radiation.

In this study, $c_{p,s}$ can be assumed as equal to $c_{p,bulk}$ because Figure 4.11 shows temperature gradient of the sand particles at different elevations are almost same and it means solid phase can be accepted as lumped instead of inter particles. Gas radiation is also can be ignored due to low emissivity of gas [27].

Thermal discharge efficiency of this process based on the First Law of Thermodynamics can be defined as

$$\eta = \frac{\text{Thermal energy transmitted to the air}}{\text{Thermal energy in solid particles}} \quad (14)$$

Figure 4.16 shows efficiency variations for different times in experimental and CFD studies. The experimental efficiency values are higher than the CFD results. It is probably originated from the higher heat loss in CFD studies. Also, these efficiency ratios are lower than the expected amounts. Efficiency can be increased with higher initial air temperature and better sealing of the fluidized bed.

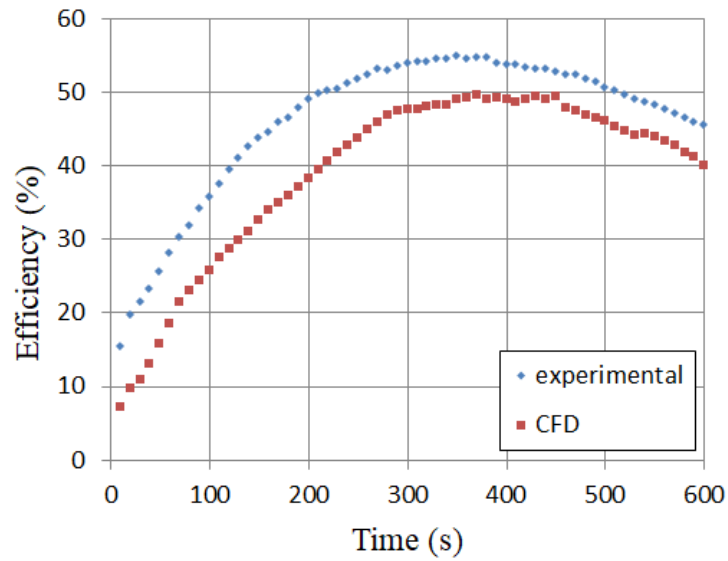


Figure 4.16 Heat transfer efficiency between phases for different studies

As mentioned before, a fluidized bed system was tested experimentally and simulated via the Ansys Fluent tool. Because of persistent fluctuations during experiments, an absolute accurate comparison between these different studies is not possible even though the results and tendencies of the changes are supporting each other. CFD studies supply more details and more data than experiments because during experiments results can be obtained for everywhere in the domain. The disadvantage of the numerical study is that some important properties must be set for the entire bed uniformly. Finally, it can be concluded that experimental results mostly reflect the truth better than the CFD results.

CHAPTER 5

CONCLUSIONS

The main motivation behind this fluidized bed study is preparing a substructure for developing the energy storage components in CSP systems. Thanks to this, higher availability and efficiency plants with thermal energy storage can be built with the production of lower-cost electricity. In this direction, the numerical study of Hiçdurmaz [19][29] was validated experimentally. There are some other studies in the literature similar to this study. The most comparable one include similar hydrodynamical set-ups and numerical approaches. Nevertheless, this study differs from the others with the included thermal experimental study.

Fluidized bed systems can be created with different heat storage mediums; sensible, chemical and latent. Silica sand from sensible heat storage group was chosen in this case because of the advantages as stability at high temperatures, no need for heat exchanger and not a dangerous material. Besides these low cost and availability are other important factors if this plant will be in a desert area, the cost approaches to zero. This study realized with a bed with dimensions 0.08 m x 0.4 m x 0.08 m and granular particles were categorized in Geldart B type particles with 600 μm .

System modeled and experimented hydrodynamically and thermally. The model was built in ANSYS Fluent 17.2 with the help of the Syamlal O'Brien drag model and the Gunn thermal model. Also, for the multiphase structure Eulerian-Eulerian approach was applied. In the first part of experiments and simulations, hydrodynamic behaviors of the bed were validated with the data of pressure drop across the bed and bed expansion ratio and results adjusted with each other. Pressure drop was measured by the help of two manometers from the bottom and top of the bed and bed expansion estimated with eyeball method. Experiments were

repeated with CARBOHSP particles and hydrodynamic results show that these particles have better fluidization inclination than sand particles. The pressure drop across the bed is stable with different superficial velocities because of the pressure definition and the bed height ratio increases with higher superficial velocities.

In both experimental studies, air was used at room temperature for fluid regime but sand was at room temperature only in the hydrodynamic part. Its initial temperature is around 585 K in the second part of experiments. In the second part of the study, interphase heat transfer coefficient and temperature of the sand and air were studied. Also, CARBOHSP and, sand particles were compared experimentally and these performed similar cooling behaviors. Temperature gradient was determined by K-type thermocouples at different elevations. Diagram of heat transfer coefficient demonstrated that when the measuring point height increases, heat transfer coefficient decreases and values linearly change with temperature values.

The most important difference between Hiçdurmaz's study is air-sand temperature gradients during discharging processes. Instead of both phases have almost the same temperature after a short time in these study temperatures comes to equilibrium after 550 s. The strongest reasons behind this variation are using different bed geometry and heat losses from the wall in reality. Heat losses from the walls are not considered in his thesis because the study was established for integrating the unit with Ivanpah Solar Power Plant with multiple packing units.

Causes of the few small differences between results may be originated from the filters which are fitted at the locations under the lower manometer and over the higher manometer. These filters must be used to prevent the particles escaping from the bed, but they led to some extra pressure drop in the bed. In thermal results, the heat losses from the insulation and inability to predict the thermal contact resistance may be the causes of the observed deviations.

5.1. Future Work

In the future, to improve the technology readiness of the investigated thermal energy storage concept,

- Experiments may be conducted at higher temperatures with proper equipment,
- Different granular particles may be investigated if they provide higher efficiency that can overcome the higher costs of particles.
- The proposed thermal energy storage module may be tested coupling it with a solar receiver that can supply the hot particles.

REFERENCES

- [1] M. P. Paranthaman, W. Wong-Ng, and R. N. Bhattacharya, *Semiconductor materials for solar photovoltaic cells*. 2015.
- [2] C. C. Xu and J. Zhu, “Prediction of the minimum fluidization velocity for fine particles of various degrees of cohesiveness,” *Chem. Eng. Commun.*, vol. 196, no. 4, pp. 499–517, 2009.
- [3] “2017 Renewable Energy Data Book: Including Data and Trends for Energy Storage and Electric Vehicles ,” U.S. Dept. of Energy, January 2019.
- [4] P. Heller, *The performance of concentrated solar power (CSP) systems : analysis, measurement and assessment. ,* 2017.
- [5] “10.2. Parabolic Trough Collector Systems | EME 811: Solar Thermal Energy for Utilities and Industry.” [Online]. Available: <https://www.eeducation.psu.edu/eme811/node/683>. [Accessed: 26-May-2019].
- [6] “Linear Fresnel systems and the future for Concentrated Solar Power – HELIOSCSP.” [Online]. Available: <http://helioscsp.com/linear-fresnel-systems-and-the-future-for-concentrated-solar-power/>. [Accessed: 27-May-2019].
- [7] F. Vejahati, N. Mahinpey, N. Ellis, and M. B. Nikoo, “CFD simulation of gas-solid bubbling fluidized bed: A new method for adjusting drag law,” *Can. J. Chem. Eng.*, vol. 87, no. 1, pp. 19–30, 2009.
- [8] J. Coventry and C. Andraka, “Dish systems for CSP,” *Sol. Energy*, vol. 152, pp. 140–170, Aug. 2017.

- [9] G. Alva, Y. Lin, and G. Fang, “An overview of thermal energy storage systems,” *Energy*, vol. 144, pp. 341–378, 2018.
- [10] “Concentrated Solar Power (CSP) – How it Works – HELIOSCSP.” [Online]. Available: <http://helioscsp.com/concentrated-solar-power-csp-how-it-works/>. [Accessed: 30-May-2019].
- [11] Z. Ma, G. C. Glatzmaier, and M. Mehos, “Development of solid particle thermal energy storage for concentrating solar power plants that use fluidized bed technology,” *Energy Procedia*, vol. 49, pp. 898–907, 2013.
- [12] S. Warekar, S. Schmitz, J. Goettsche, B. Hoffschmidt, M. Reißel, and R. Tamme, “Air-Sand Heat Exchanger for High-Temperature Storage,” *J. Sol. Energy Eng.*, vol. 133, pp. 1–8, 2011.
- [13] T. Baumann, S. Zunft, and R. Tamme, “Moving Bed Heat Exchangers for Use With Heat Storage in Concentrating Solar Plants: A Multiphase Model,” *Heat Transf. Eng.*, vol. 35, no. 3, pp. 1–8, 2014.
- [14] H. Brenner, A. Acrivos, J. E. Bailey, and L. Fan, *Butterworth-Heinemann Series in Chemical Engineering*. 2013.
- [15] R. Cocco, S. B. R. Karri, and T. Knowlton, “Introduction to fluidization,” *Chem. Eng. Prog.*, vol. 110, no. 11, pp. 21–29, 2014.
- [16] L. Ruhanen, “Chapter 2. Introduction to Australia,” *Oceania*, pp. 7–16, 2018.
- [17] W.-C. Yang, “Particle Characterization and Dynamics,” in *Handbook of fluidization and fluid-particles systems*, New York, 2003.
- [18] R. J. Moffat, “Describing the uncertainties in experimental results,” *Exp. Therm. Fluid Sci.*, vol. 1, no. 1, pp. 3–17, 1988.
- [19] Serdar Hiçdurmaz, “Numerical Investigation of Bubbling Fluidized Bed To Be Used as High Temperature Thermal Energy Storage,” no. July, 2017.

- [20] F. Taghipour, N. Ellis, and C. Wong, "Experimental and computational study of gas-solid fluidized bed hydrodynamics," *Chem. Eng. Sci.*, vol. 60, no. 24, pp. 6857–6867, 2005.
- [21] M. Syamlal and T. J. O'Brien, "Fluid dynamic simulation of O-3 decomposition in a bubbling fluidized bed," *Aiche J.*, vol. 49, no. 11, pp. 2793–2801, 2003.
- [22] E. Peirano, V. Delloume, and B. Leckner, "Two- or three-dimensional simulations of turbulent gas-solid flows applied to fluidization," *Chem. Eng. Sci.*, vol. 56, pp. 4787–4799, 2001.
- [23] D. J. Gunn, "Transfer of heat or mass to particles in fixed and fluidised beds," *Int. J. Heat Mass Transf.*, vol. 21, no. 4, pp. 467–476, 1978.
- [24] D. Gidaspow, *Multiphase flow and fluidization - Continuum and Kinetic Theory Descriptions*. 1994.
- [25] D. Geldart, "Expansion of gas fluidized beds," *Ind. Eng. Chem. Res.*, vol. 43, no. 18, pp. 5802–5809, 2004.
- [26] A. Pare, "Hydrodynamics of Three Phase Fluidized Bed Using Low Density Particles Department of Chemical Engineering National Institute of Technology Rourkela Bed Using Low Density Particles," 2013.
- [27] Z. Zhou, Q. Hou, and A. Yu, "Particle Scale Simulation of Heat Transfer in Fluid Bed Reactors," *Heat Transf. - Math. Model. Numer. Methods Inf. Technol.*, 2011.
- [28] N. P. Siegel, M. D. Gross, and R. Coury, "The development of direct absorption and storage media for falling particle solar central receivers," *J. Sol. Energy Eng. Trans. ASME*, vol. 137, no. 4, 2015.

- [29] S. Hicdurmaz and I. Tari, “Numerical investigation of bubbling fluidized bed to be used as thermal energy storage integrated to high-temperature concentrated solar power,” *Multiph. Sci. Technol.*, vol. 30, no. 2–3, pp. 99–120, 2018.
- [30] S. Pannala, M. Syamlal, and T. J. O’Brien, *Computational Gas-Solids Flows and Reacting Systems- Theory, Methods and Practice*. New York, 2011.

APPENDICES

A. Experimental Temperature (K) Variation of Sand Particles at Different Elevations for First 340 s , U=0.38

	y=0.05 m	y=0.10 m	y=0.20 m	y=0.35 m
2	586	577	421	361
4	586	576	408	354
6	585	576	404	355
8	567	574	457	399
10	560	575	448	389
12	557	575	438	382
14	556	573	429	377
16	556	573	421	372
18	555	572	414	369
20	553	571	408	366
22	553	571	402	364
24	553	570	398	361
26	553	570	396	359
28	551	569	392	357
30	551	568	389	356
32	552	568	387	354
34	551	568	386	354
36	551	568	385	354
38	551	567	383	353
40	550	567	381	353
42	549	566	381	353
44	549	566	380	352
46	549	566	380	352
48	549	566	380	352
50	548	565	381	352
52	547	565	382	352
54	547	565	384	353
56	547	565	384	353
58	547	564	422	380

60	552	564	462	409
62	541	551	477	419
64	537	550	483	419
66	534	546	485	420
68	533	545	487	422
70	531	545	487	422
72	529	545	488	423
74	528	542	490	424
76	526	539	492	426
78	525	537	493	428
80	524	535	493	429
82	522	533	494	431
84	522	531	494	432
86	522	530	494	432
88	523	528	494	432
90	523	527	493	431
92	523	527	493	433
94	523	526	493	432
96	522	525	493	430
98	521	523	493	432
100	520	522	493	431
102	519	522	492	431
104	518	520	492	431
106	518	518	492	430
108	518	517	491	429
110	517	516	491	430
112	516	515	491	431
114	516	515	490	431
116	516	514	490	431
118	514	512	490	430
120	513	512	490	430
122	512	511	490	431
124	511	510	489	431
126	510	509	489	430
128	509	508	489	431
130	508	507	488	433
132	506	506	488	434
134	505	505	488	434

136	505	505	487	434
138	505	505	487	435
140	505	503	486	434
142	503	502	486	434
144	501	502	485	435
146	501	502	485	435
148	500	500	484	434
150	498	500	484	434
152	498	499	484	433
154	498	499	483	433
156	497	498	483	434
158	497	498	482	433
160	496	496	482	434
162	495	496	482	432
164	495	495	482	433
166	493	495	481	434
168	493	494	481	435
170	491	493	480	434
172	492	493	480	434
174	492	492	480	433
176	491	491	480	433
178	490	491	479	434
180	490	490	479	434
182	489	490	478	434
184	488	489	478	434
186	487	489	477	434
188	487	488	477	434
190	487	488	477	433
192	486	487	477	434
194	486	486	476	434
196	485	486	476	432
198	485	485	475	433
200	484	485	475	434
202	482	484	475	434
204	482	483	474	432
206	483	482	474	433
208	482	481	473	432
210	481	480	472	432

212	482	479	472	432
214	482	478	471	432
216	481	478	470	432
218	480	477	470	431
220	478	476	470	431
222	477	476	469	431
224	476	475	469	431
226	476	475	468	431
228	475	474	468	431
230	474	474	468	431
232	474	473	467	431
234	474	472	466	431
236	472	472	466	430
238	472	471	465	430
240	471	471	465	430
242	471	470	465	430
244	471	470	465	429
246	470	469	464	429
248	469	469	464	429
250	469	468	464	428
252	468	468	463	429
254	468	467	463	429
256	467	467	463	428
258	467	466	462	429
260	466	466	461	428
262	466	465	461	428
264	465	465	460	428
266	464	464	460	429
268	464	464	460	428
270	463	463	460	428
272	463	463	459	428
274	462	462	459	428
276	461	462	458	427
278	461	461	458	428
280	461	461	458	427
282	461	460	458	427
284	460	459	457	427
286	460	459	457	427

288	459	459	456	426
290	459	458	456	426
292	458	458	455	426
294	457	457	455	426
296	457	457	455	426
298	457	456	454	426
300	456	455	454	426
302	456	455	454	425
304	455	455	453	425
306	455	455	452	424
308	454	454	452	424
310	454	453	452	424
312	453	453	451	424
314	452	452	451	423
316	452	452	450	423
318	451	451	450	423
320	451	451	450	422
322	450	450	449	422
324	450	450	449	422
326	449	449	448	422
328	449	449	448	422
330	448	448	447	422
332	448	448	447	422
334	447	447	446	422
336	447	447	446	421
338	447	446	445	420
340	446	446	445	420